Joint AVO analysis of PP and PS seismic data

Yong Xu and John C. Bancroft

ABSTRACT

This paper makes efforts to explore joint-analyzing the amplitude versus offset phenomena in the PP and PS data with expectation to reduce the ambiguity of AVO analysis by utilizing the redundancy of multi-component AVO measurements. The convenient approximations of P-P and P-S reflection coefficient are obtained, which link the seismic data with the elastic parameters that are sensitive to the hydrocarbon existing in the rock. A great deal of model and real data is used to test the methods.

In this paper, we derive the approximation of PS reflection coefficient from Zoeppritz equation, correct Aki and Richards's approximation, and derive some equations of PS reflection coefficient possibly easy to be used in PS AVO analysis.

We study the laboratory and well logging results, and show the difference between bulk modulus (κ) and rigidity or shear modulus (μ) is influenced by fluid-fill more purely, and it is a sensitive and quantitative indicator of gas existing.

P-P and P-S reflection coefficient equations are expressed with the elastic parameters (λ and μ, or κ and μ) in the paper. And it is shown by the well log that this kind of expression magnify the changes embedded in the Vp and is advantageous to extract the anomaly caused by fluid-fill.

The method to extract the zero offset section or approximate normal incidence section is present in the paper. The method in this paper is based on the PP reflection coefficient with only care on constant term independent of incident angles.

Wells and 10 Hz vertical component seismic data from Blackfoot, Alberta are used to test our methods and theory. We amplitude-preserved process vertical component data, and extract the elastic parameters and zero offset. We are working on the radial component data set and hope the elastic parameter extraction from radial component may support the extraction from vertical component data set.

INTRODUCTION

Amplitude versus offset relationships can be considered from a theoretical or practical standpoint. In theory, as the AVO phenomena translates the sharing of the energy of the incident compressible wave between the compressible and converted reflections, the observation of the converted mode AVO would be redundant. In practice, a few years of experience in P-mode AVO observation may lead to different conclusions. In some privileged areas, the AVO of compressible waves effectively provides the expected information. In most cases, single fold data are not pure enough to provide reliable amplitude measurements, and finally the result is doubtful. In such cases, study of the AVO of the converted mode can be advantageous: when compatible with the P-P AVO, it confirms it, and when not, it denounces unreliable information.

The Zoeppritz equations describe the reflections of incident, reflected, and transmitted P waves and S waves on both sides of an interface. For analysis of wave reflection we need an equation which relates reflected wave amplitudes to incident wave amplitudes as a function of angles of incidence. In the past decade, many forms of simplifications of Zoeppritz equation of P-P reflection coefficient appeared in the literature and industrial practice (Aki and Richards, 1980, Shuey, 1985, Parson, 1986, Smith and Gidlow, 1989, Verm and Hilterman, 1994). Each of these simplifications in a degree links reflection amplitude with variations of rock properties. Aki and Richard (1980) give the approximation of P-S reflection coefficient. There is also a rough approximation linking P-S reflection coefficient with pure SH reflection coefficient (Frasier and Winterstein, 1993, Stewart, 1995). Because of the challenges in the processing of the real radial data which are mainly P-S reflections, applications of P-S reflection coefficient and AVO analysis rarely appear in the literatures and practice. We would like to have a PS reflection coefficient equation accurate and easy to link seismic with rock property changes. In this paper, we derive the approximation of PS reflection coefficient from Zoeppritz equation, corrected Aki and Richards's approximation for great S wave property changes, and derive some forms of PS reflection coefficient equations possibly easy to be used in P-S AVO analysis.

In AVO analysis, practices mainly focus on looking for more sensitive indicator of hydrocarbon and extracting and exploiting anomalous variations between seismic and these sensitive parameters. Some authors (Goodway et al 1997) showed the advantages of converting velocity measurements to Lame's moduli parameters (λ and μ) to improve identification indicator of reservoir zones. Castagna et al (1985) observed a few relationships of compressible wave and shear wave in the clastic silicate rocks. These give us good empirical guidance to study the rock property from seismic data. We study these relationships and well logging data, and show the difference between bulk modulus and rigidity is a sensitive and quantitative indicator of gas existing.

Least square regression analysis and inversion are the common approaches in the AVO analysis. Parson (1986) obtained contrasts of three elastic parameters (λ, μ, and ρ) by pre-stack inversion. Goodway et al (1997) obtained the Vp and Vs from inversion and converted them to the λ/μ to detect the reservoirs. However, the nonuniqueness is always the problem in the seismic inversion. The background velocity error causes the ratio to change greatly or eliminates the high frequency contrast. Appropriate selection of parameters, background velocity, wavelet estimation, application of a priori information are still important issues which remain to be resolved. Here we choose the least square regression analysis to extract elastic parameters from pre-stack data. The extraction provides band-limited information on which we attempt to discover anomaly caused by hydrocarbon reservoirs. And we also invert the band-limited result by recursive inversion and model-based inversion. In the regression analysis, we express the P-P and P-S reflection coefficient equations with the elastic parameters (λ and μ, or κ and μ) and extract these parameters directly without conversion from velocity.

Because of drawbacks in seismic methods such as the band-limited feature and noise level, we are always trying to obtain information from different approaches and interpret it comprehensively. The zero offset section obtained by linear regression of pre-stack data provides a better approximation to the normal incidence P-wave reflection coefficient and broader bandwidth and higher resolution. The values of triangular functions of incident and reflected angles are usually necessary in AVO parameter extraction from seismic data. However, the big errors of obtaining interval velocity from rms velocity and computation costs of ray tracing are raised. The method in this paper is based on the P-P reflection coefficient with only care on constant term independent of incident angles. The analysis can be done in t-x or f-x domains without computation of ray parameters or incident angles.

Multi-component data were acquired from Blackfoot, Alberta. In this paper, wells and 10 Hz vertical component seismic data are used to test our methods. In this paper, the difficulties in the P-S data processing are discussed. We are working on the radial component data processing. The results will hopefully be shown soon.

APPROXIMATION OF P-S REFLECTION COEFFICIENT

Approximations of the Zoeppritz equations

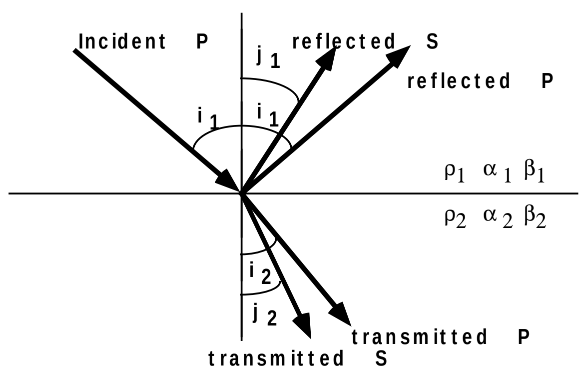

Figure 1**.** Waves generated at an interface by an incident P-wave

Figure 1 illustrates the wave propagation of incidence of compressible wave at solid-solid interface. Aki and Richards (1980) gave the approximations of P-P and P-S reflection coefficients (referred as RCs later) from Zoeppritz equations (see Appendix).

$$PP = \frac{1}{2}(1-4\beta^2 p^2)\frac{\Delta\rho}{\rho} + \frac{1}{2\cos^2 i}\frac{\Delta\alpha}{\alpha} - 4\beta^2 p^2 \frac{\Delta\beta}{\beta} \tag{1}$$

$$PS = \frac{-p\alpha}{2\cos j}[(1-2\beta^2 p^2 + 2\beta^2 \frac{\cos i}{\alpha}\frac{\cos j}{\beta})\frac{\Delta\rho}{\rho}$$

$$-(4\beta^2 p^2 - 4\beta^2 \frac{\cos i}{\alpha} \frac{\cos j}{\beta}) \frac{\Delta\beta}{\beta}] \tag{2}$$

The elastic properties in above equations are related as follows to those on each side of the interface:

$$\Delta\alpha = (\alpha_2 - \alpha_1)\,,\ \alpha = (\alpha_2 + \alpha_1)/2\,, \tag{3}$$

$$\Delta\beta = (\beta_2 - \beta_1)\,,\ \beta = (\beta_2 + \beta_1)/2\,, \tag{4}$$

and

$$\Delta\rho = (\rho_2 - \rho_1)\,,\ \rho = (\rho_2 + \rho_1)/2\,. \tag{5}$$

The angle i is the average of incident and transmitted P-wave angles while j is the average of reflected and transmitted S-wave angles:

$$i = (i_1 + i_2)/2 \quad \text{and} \quad j = (j_1 + j_2)/2\,. \tag{6}$$

Accuracy of P-S RC approximations

Ostrander (1984) devised a hypothetical gas sand model to analyze plane-wave reflection coefficients as a function of angle of incidence. Figure 2 shows Ostrander's model, a three layer gas sand model with parameters which might be typical for a shallow, young geologic section. Here, gas sand with a Poisson's ratio of 0.1 is embedded in shale having a Poisson's ratio of 0.4. There is a 20 percent P-wave velocity reduction going into the sand, from 10,000 ft/s to 8,000 ft/s, and a 10 percent density reduction from 2.40 g/cm^3 to 2.14 g/cm^3. The Poisson's ratio is changed to 0.4 if there is no gas in the sand layer. This would simulate the case of low-velocity brine-saturated young sandstone embedded in shale.

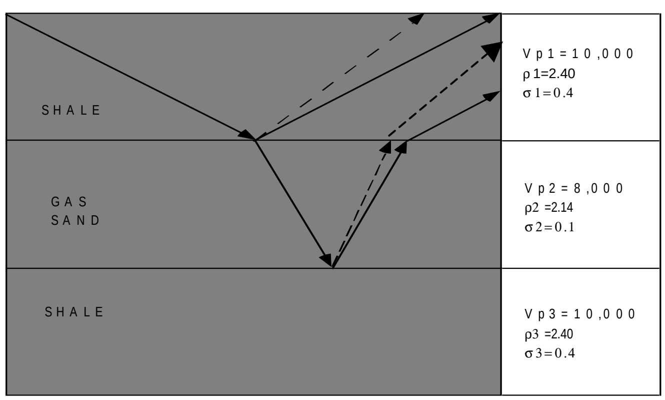

Figure 2. Three-layer hypothetical gas sand model (Ostrander, 1984)

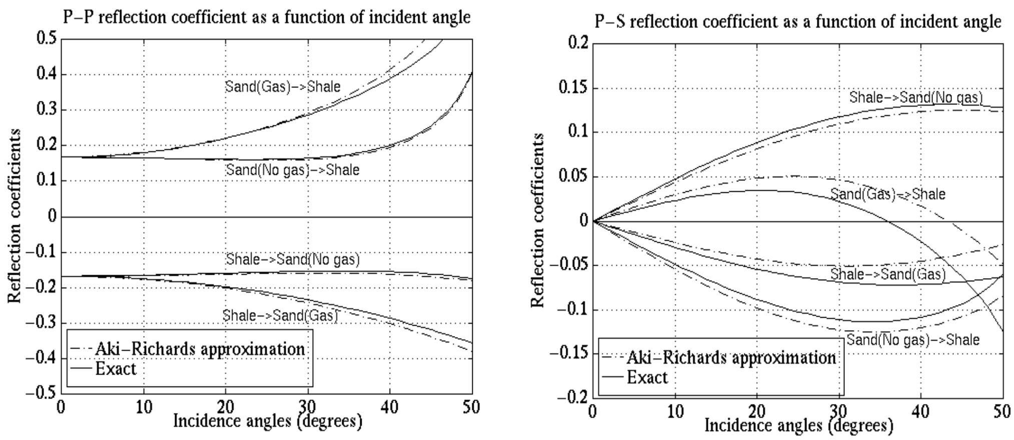

(a) (b)

Figure 3. The exact and approximated reflection coefficients in the media with elastic properties specified in Figure 2**.**

In Figure 3, the exact and approximated reflection coefficients are compared in the media with elastic properties specified in Figure 2. The solid lines are for the exact and the dash lines are for Aki-Richards approximations. Here, the cases without gas in the sand of second layer in Figure 2 are shown also, in which the Poisson ratio is of 0.4. Panel (a) shows P-P reflection coefficients for the two interfaces in Figure 2 and for two cases--with and without gas in the sand. Panel (b) shows P-S reflection coefficients for the two interfaces in Figure 2 and for two cases--with and without gas in the sand. After comparing panel (a) and panel (b), we observe three points:

- At normal incidence on the interface with elastic property variation, P-S reflection coefficient is zero and P-P reflection coefficient is not zero.
- In the small incident angle case, the magnitude of P-P reflection coefficient is bigger than magnitude of P-S reflection coefficient.
- Aki-Richards approximation of P-S reflection coefficient, equation (2) has bigger relative error than the approximation of P-P reflection coefficient, equation (1) in the model cases in Figure 2, especially the gas-filled sand cases. It is necessary to correct the Aki-Richards approximation of P-S reflection coefficient.

Under the definitions (3), (4), (5) and (6) with truncation after $(\frac{\Delta\alpha}{\alpha})^2, (\frac{\Delta\beta}{\beta})^2, \frac{\Delta\alpha}{\alpha}\frac{\Delta\beta}{\beta}, \frac{\Delta\alpha}{\alpha}\frac{\Delta\rho}{\rho}, \frac{\Delta\beta}{\beta}\frac{\Delta\rho}{\rho}$, and $(\frac{\Delta\rho}{\rho})^2$, after expanding the exact reflection coefficient from Zoeppritz equations (see Appendix), the higher order approximations for P-S reflection coefficient should be:

$$PS = A[C_1 \frac{\Delta\rho}{\rho} + C_2 \frac{\Delta\beta}{\beta} + D_1 (\frac{\Delta\rho}{\rho})^2 + D_2 (\frac{\Delta\rho}{\rho}\frac{\Delta\alpha}{\alpha}) + D_3 (\frac{\Delta\rho}{\rho}\frac{\Delta\beta}{\beta}) + D_4 (\frac{\Delta\alpha}{\alpha}\frac{\Delta\beta}{\beta}) + D_5 (\frac{\Delta\beta}{\beta})^2] \quad (7)$$

where

$$A = -\frac{1}{2}\frac{\sin i}{\cos j} \ ,$$

$$C_1 = 1 - 2\sin^2 j + 2\frac{\beta}{\alpha}\cos i \cos j \ ,$$

$$C_2 = -(4\sin^2 j - 4\frac{\beta}{\alpha}\cos i \cos j) \ ,$$

$$D_1 = \frac{1}{2} - 3\sin^2 j - \frac{\beta}{\alpha}\cos i \cos j - 4\frac{\beta}{\alpha}\sin^2 j \cos(i-j) \ ,$$

$$D_2 = \frac{1}{2}\tan^2 i \cos 2j - \frac{\beta}{\alpha}\cos i \cos j \ ,$$

$$D_3 = \frac{1}{2} + 16\frac{\beta}{\alpha}\sin^2 j \cos(i-j) - \frac{\beta}{\alpha}\frac{\cos i}{\cos j}(1+\cos^2 j) - 7\sin^2 j \ ,$$

$$D_4 = -2\tan^2 i \sin^2 j - 2\frac{\beta}{\alpha}\cos i \cos j \ ,$$

and

$$D_5 = 5\sin^2 j \ .$$

The accuracy of equation (7) are compared with the accuracies of Zoeppritz equation, and Aki-Richards approximation--equation (2) in Figure 4, in which the reflection coefficients and relative errors of approximations versus incident angle are plotted. In Figure 4, the later equation (12) and equation (13) are also plotted.

Aki-Richards approximation--equation (2) can be rewritten as polynomial of $\cos(i+j)$ or $\sin^2 j$ as equation (8) and equation (9).

$$PS = A[P_0 + P_1 \cos(i+j)] \quad (8)$$

where

$$A = -\frac{\sin i}{2\cos j} = -\frac{1}{2}\frac{\alpha}{\beta}\tan j\,,\ P_0 = \frac{\Delta\rho}{\rho}\,,\ P_1 = 2\frac{\beta}{\alpha}B\,,\text{ and }\ B = \frac{\Delta\rho}{\rho} + 2\frac{\Delta\beta}{\beta}\,.$$

With Snell's law and truncation after $\sin^6 j$, equation (8) is expanded as:

$$PS = A[C_0 + C_1 \sin^2 j + C_2 \sin^4 j] \tag{9}$$

where

$$C_0 = \frac{\Delta\rho}{\rho} + 2\frac{\beta}{\alpha}B\,,\ C_1 = -\frac{\beta}{\alpha}B(\frac{\alpha}{\beta}+1)^2\,,\text{ and }\ C_2 = -\frac{1}{4}\frac{\beta}{\alpha}B(\frac{\alpha^2}{\beta^2}+1)^2\,.$$

Further approximation of equation (9) by dropping the $\sin^4 j$ term is the following equation (10), and its accuracy is as good as that of equation (9) for the small and intermediate incident angles.

$$PS = A(C_0 + C_1 \sin^2 j) \tag{10}$$

Expand A in term of sin$j$, then we have:

$$PS = D_1 \sin j + D_2 \sin^3 j \tag{11}$$

where

$$D_1 = -\frac{1}{2}\frac{\alpha}{\beta}C_0\,,\text{ and } D_2 = -\frac{1}{2}\frac{\alpha}{\beta}(\frac{1}{2}C_0 + C_1)\,.$$

From comparisons of the curves in Figure 4, we find that the Aki-Richards approximations of P-S reflection coefficient as equation (2) or equation (8) are not accurate enough. Figure 5 compares equation (2), equation (7) after divided by tan$j$, and we find the error of Aki-Richards approximation is great in the near normal incidence. Using equation (7), we can correct equation (8) and equation (9). If only P_0 in equation (8) and C_0 in equation (9) are corrected, the approximations could be more accurate than equation (2)--the Aki-Richards approximation. Equation (12) and equation (13) as follows are the corrected formulas:

$$PS = A[P_0 + P_1 \cos(i + j)] \tag{12}$$

where

$$A = -\frac{\sin i}{2\cos j} = -\frac{1}{2}\frac{\alpha}{\beta}\tan j\,,$$

$$P_0 = \frac{\Delta\rho}{\rho}(1 + R_{ss}) - 2\frac{\beta}{\alpha}BR_{pp}\ \ ,$$

$$P_1 = 2\frac{\beta}{\alpha}B,$$

$$R_{ss} = \frac{1}{2}(\frac{\Delta\rho}{\rho} + \frac{\Delta\beta}{\beta}),$$

$$R_{pp} = \frac{1}{2}(\frac{\Delta\rho}{\rho} + \frac{\Delta\alpha}{\alpha}),$$

and

$$B = \frac{\Delta\rho}{\rho} + 2\frac{\Delta\beta}{\beta} = 2R_{ss} + \frac{\Delta\beta}{\beta}.$$

$$PS = A[C_0 + C_1 \sin^2 j + C_2 \sin^4 j] \tag{13}$$

where

$$C_0 = \frac{\Delta\rho}{\rho}(1 + R_{ss}) + 2\frac{\beta}{\alpha}B(1 - R_{pp}),$$

$$C_1 = -\frac{\beta}{\alpha}B(\frac{\alpha}{\beta} + 1)^2, \text{ and } C_2 = -\frac{1}{4}\frac{\beta}{\alpha}B(\frac{\alpha^2}{\beta^2} + 1)^2.$$

In Figure 4 and Figure 5, equation (12) and equation (13) are compared with Aki-Richards approximation, equation (7) and the exact.

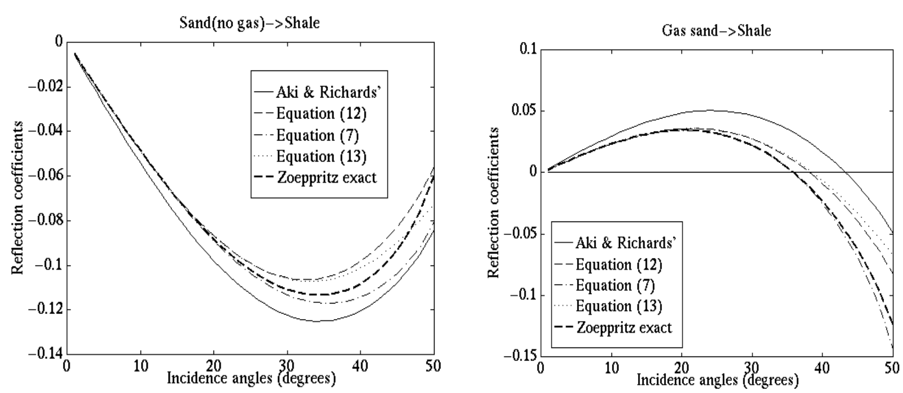

(a) (b)

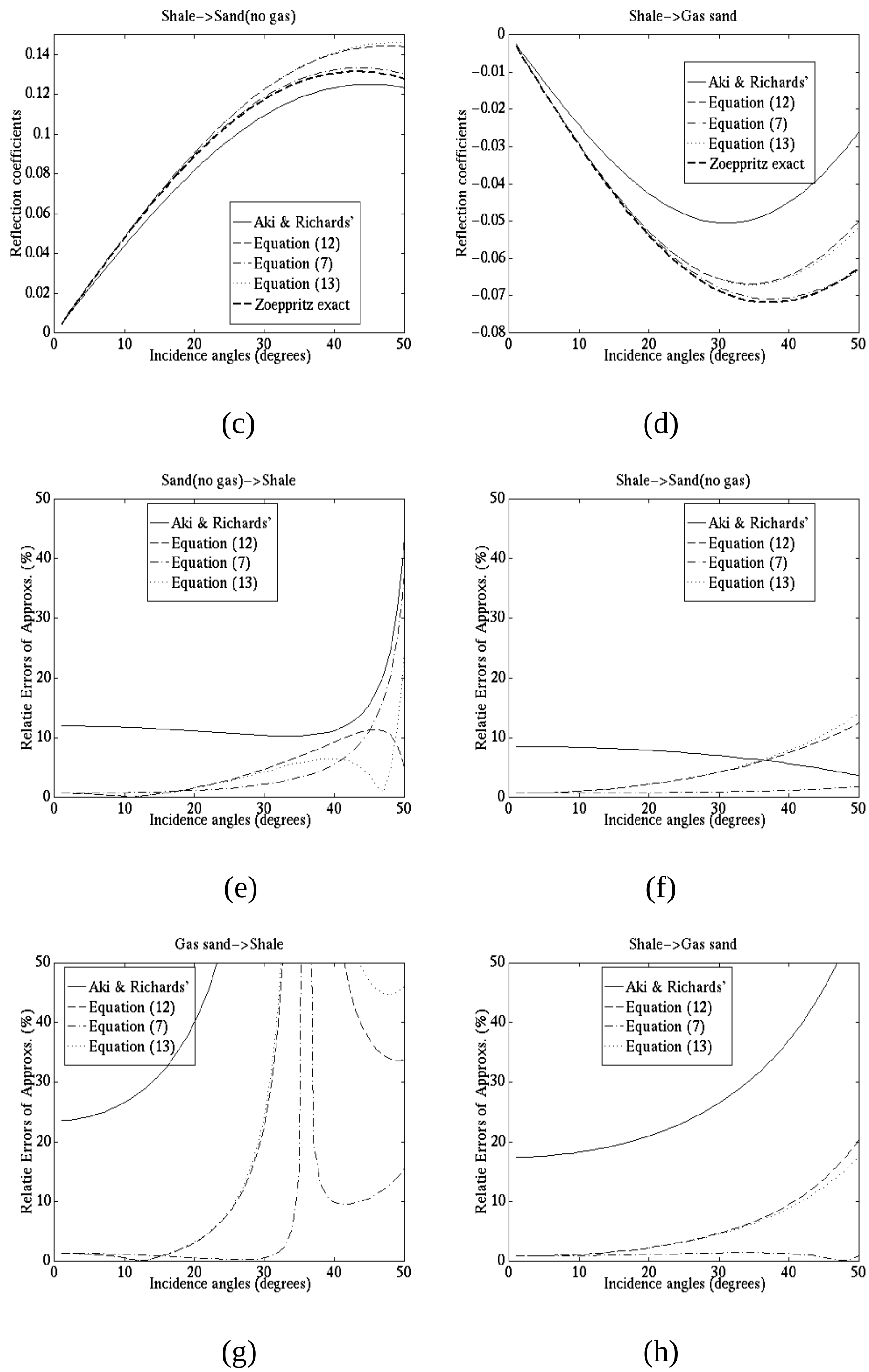

Figure 4. Comparisons of the exact P-S reflection coefficients, Aki-Richards approximation (2), equation (7), equation (12) and equation (13) for the three-layer sand model in Figure 2. (a), (b), (c), and (d) are the reflection coefficients versus incident angles. (e), (f), (g), and (h) are the relative errors versus incident angles.

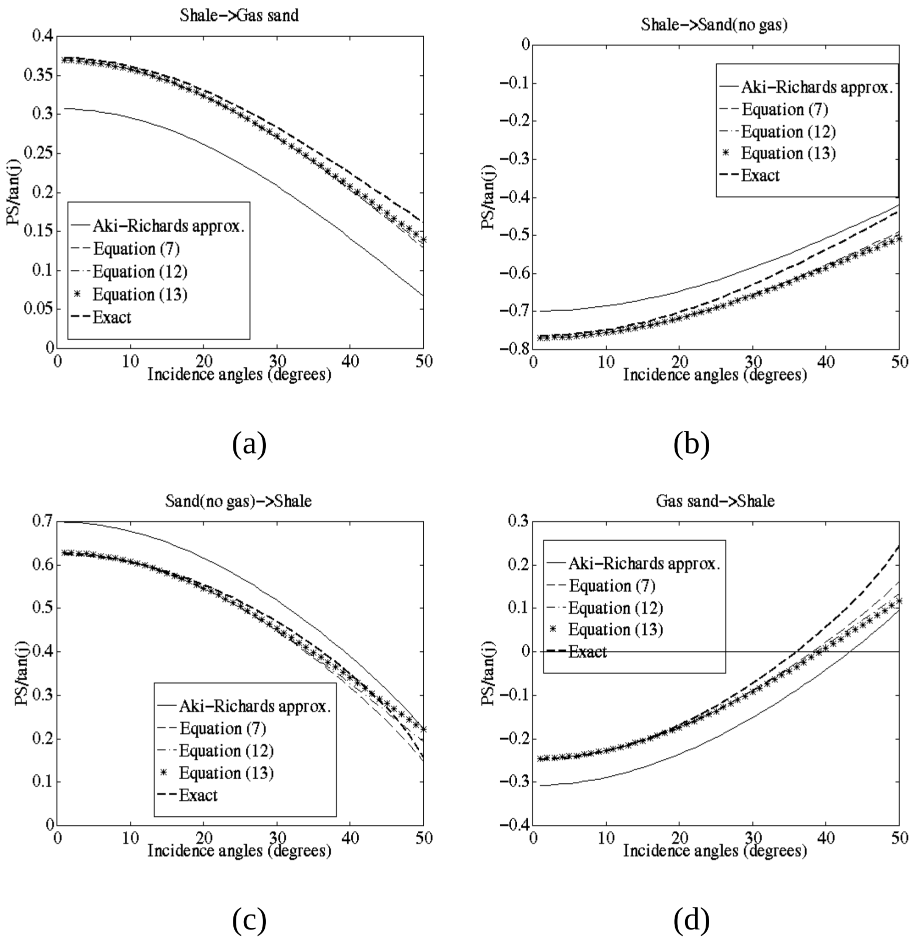

Figure 5. Plots of equations (2), (7), (12) and (13) after divided by tan*j* versus incident angle.

The model used in Figure 2 is a young gas sand model with big S wave property change at the interface. Now investigate another gas sand model with properties of overburden shale and gas sand in Table 1. This model is common case to generate the P-P AVO anomaly and may be classified as Class III (Rutherford and Williams, 1989).

Table 1 Property of second gas sand model**.**

	Vp	Vs	Density
Shale	3811	2263	2.40
Gas sand	3453	2302	2.10

Figure 6 shows the comparison of approximations and exact reflection coefficients for this model in Table 1. The Aki-Richards' approximation is good enough for this model in which shear wave velocities have smaller changes.

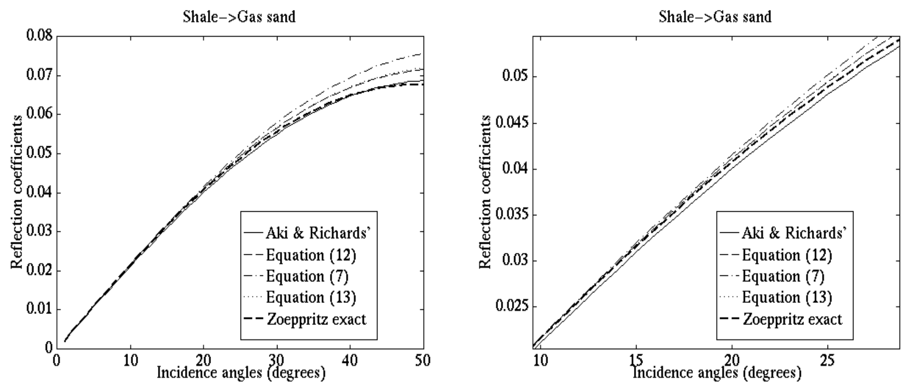

(a) P-S reflection coefficients (b) enlargement of part of (a)

Figure 6. Comparison of approximation and exact reflection coefficients for gas sand model in Table 1.

The average relative errors of Aki-Richards' approximation for P-S reflection coefficients on the interfaces of the macro layers extracted from 08-08 well in Blackfoot survey (Figure 7) are calculated. The incident angle range is 1-40 degrees. Except the top of Mississippian, most of the relative error is less than 10% (The biggest is 7.5%).

After tested by different models, the Aki-Richards approximation of P-S reflection coefficient can be regarded good for the small incident angles and small S wave property changes. The error of this approximation would be tolerant for a great part of cases in the real world.

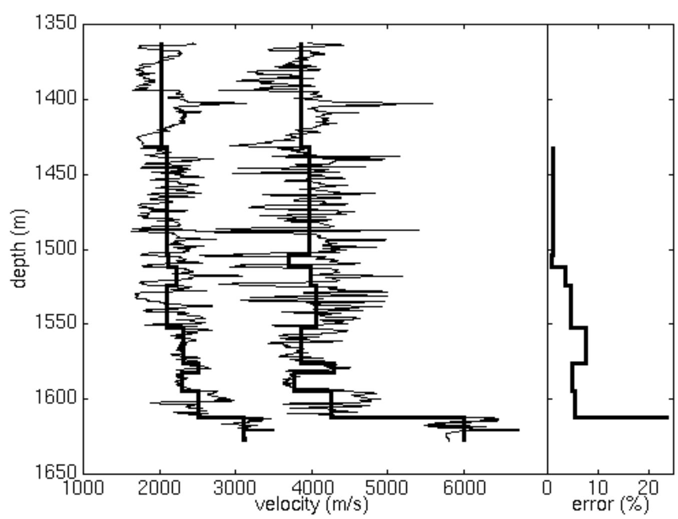

Figure 7. The average relative error of macro layers from well logs (Blackfoot 0808 well).

Relationship between PS and SS

Stewart (1995) showed an approximate relationship between converted-wave reflectivity *PS* and pure SH reflectivity *SS*. The equation that approximates the pure SH reflectivity is given (Aki and Richards, 1980) as:

$$SS = -\frac{1}{2}(1-4\beta^2 p^2)\frac{\Delta\rho}{\rho} - (\frac{1}{2\cos^2 j} - 4\beta^2 p^2)\frac{\Delta\beta}{\beta} \tag{14}$$

The relationship between converted-wave reflectivity *PS* and pure S reflectivity *SS* is as:

$$PS = -\frac{p\alpha}{2\cos j}[-8\frac{\beta}{\alpha}SS + (1-2\frac{\beta}{\alpha})\frac{\Delta\rho}{\rho}] \tag{15}$$

Now as $\frac{\beta}{\alpha} \sim \frac{1}{2}$, the second term in the equation (15) is very small. Thus

$$PS \sim 4\sin j\, SS_0 \tag{16}$$

Where

$$SS_0 = -\frac{1}{2}(\frac{\Delta\rho}{\rho} + \frac{\Delta\beta}{\beta})$$

With the hypothetical model in Figure 2, the exact P-S reflection coefficients, Aki-Richards approximations, and higher order approximation--equation (7) and equation (15) are compared. Figure 8 shows comparisons of the P-S reflection coefficients of equation (2), (7), and (15) as a function of incident angle. And the gas sand model in Table 1 is also used to test the equation (15) and the comparison is shown in Figure 9.

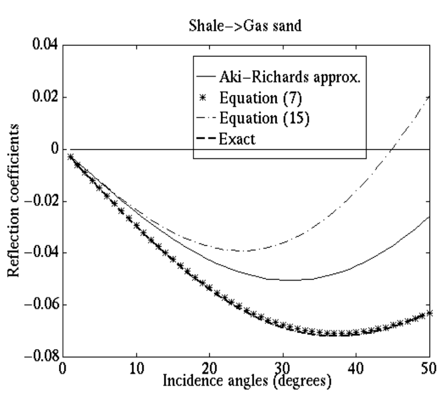

(a)

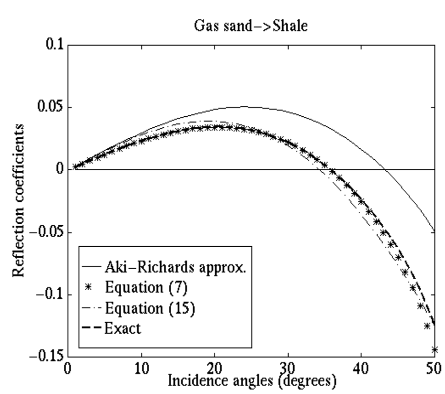

(b)

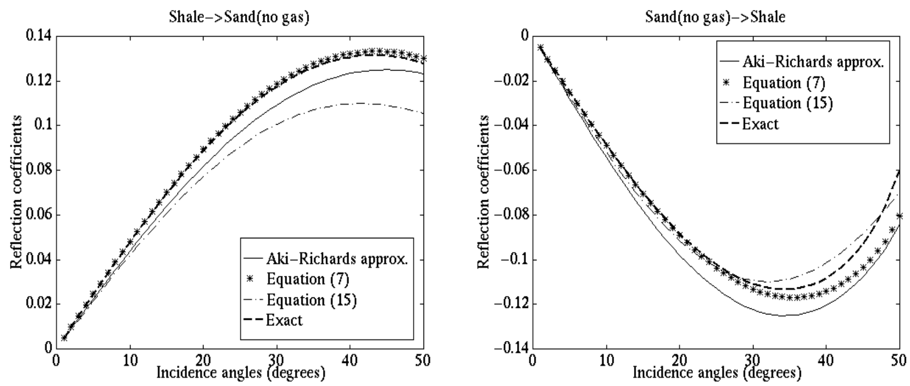

(c) (d)

Figure 8. Comparisons of P-S reflection coefficients in equation (7), Aki-Richards approximation—equation (2), equation (7), and equation (15) --relationship between *PS* and *SS*. The four panels are the P-S reflection coefficients versus angle of incidence for the three-layer sand model in Figure 2.

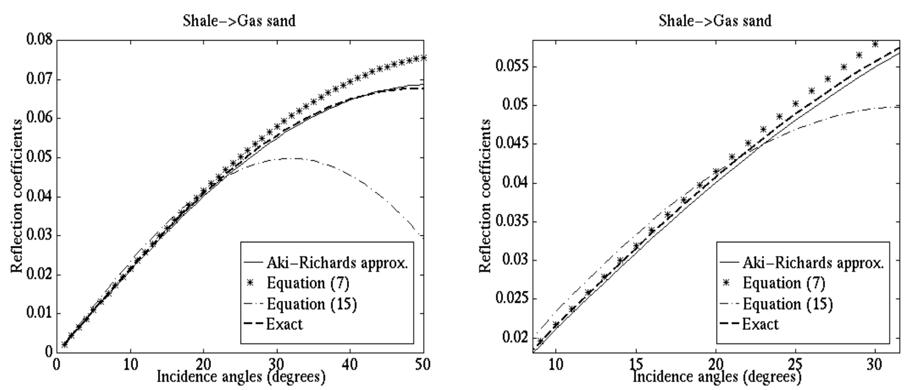

(a) Reflection coefficients (b) enlargement of part of (a)

Figure 9. Comparison of approximation and exact reflection coefficients for gas sand model in Table 1.

$\kappa-\mu$ AS DIRECT HYDROCARBON INDICATOR

Stewart (1995) advised that λ/μ might have less influence of lithology and highlight pore-fill changes. Goodway et al. (1997) observed the conversion from velocity measurements to Lame's moduli parameters of rigidity (μ) and incompressibility (λ) improves identification of reservoir zones. And cases show the moduli ratio of λ/μ is a sensitive hydrocarbon indicator. In the following, we also discuss the hydrocarbon indication of elastic parameters—κ,λ, and μ, and observe some interesting points.

Dry rock line

Castagna et al. (1985) showed the relationships between compressible-wave and shear-wave velocities in clastic silicate rocks. Here some points are quoted:

(1) Gassmann's equations are

$$\kappa_W = \kappa_S \frac{\kappa_D + Q}{\kappa_S + Q}, \tag{17a}$$

$$Q = \frac{\kappa_F(\kappa_S - \kappa_D)}{\phi(\kappa_S - \kappa_F)}, \tag{17b}$$

$$\mu_W = \mu_D, \tag{17c}$$

and

$$\rho_W = \phi\rho_F + (1-\phi)\rho_S, \tag{17d}$$

where κ_W is the bulk modulus of the wet rock, κ_S is the bulk modulus of the grains, κ_D is the bulk modulus of the dry frame, κ_F is the bulk modulus of the fluid, μ_W is the shear modulus of the wet rock, μ_D is the shear modulus of the dry rock, ρ_W is the density of the wet rock, ρ_F is the density of the fluid, ρ_S is the density of the grains, and ϕ is the porosity.

(2) As in Figure 10 (a), the dry line established with laboratory data (Vp/Vs > 1.5) means that dry bulk modulus (κ_D) is approximately equal to dry rigidity (μ_D)

$$\mu_D \approx \kappa_D \tag{18}$$

These are exactly equal when

$$V_P^D / V_S^D = 1.53 \tag{19}$$

From equation (17c) it follows that

$$\kappa_D \approx \mu_D = \mu_W \tag{20}$$

The Poisson's ratio is close to 0.1 in the dry rock and independent of P wave velocity (see Figure 10 b).

(3) Water saturation causes the bulk modulus to increase. This effect is most pronounced at higher porosities (lower moduli). Water-saturated bulk modulus normalized by density is linearly related to compressible velocity (see Figure 10 (c)).

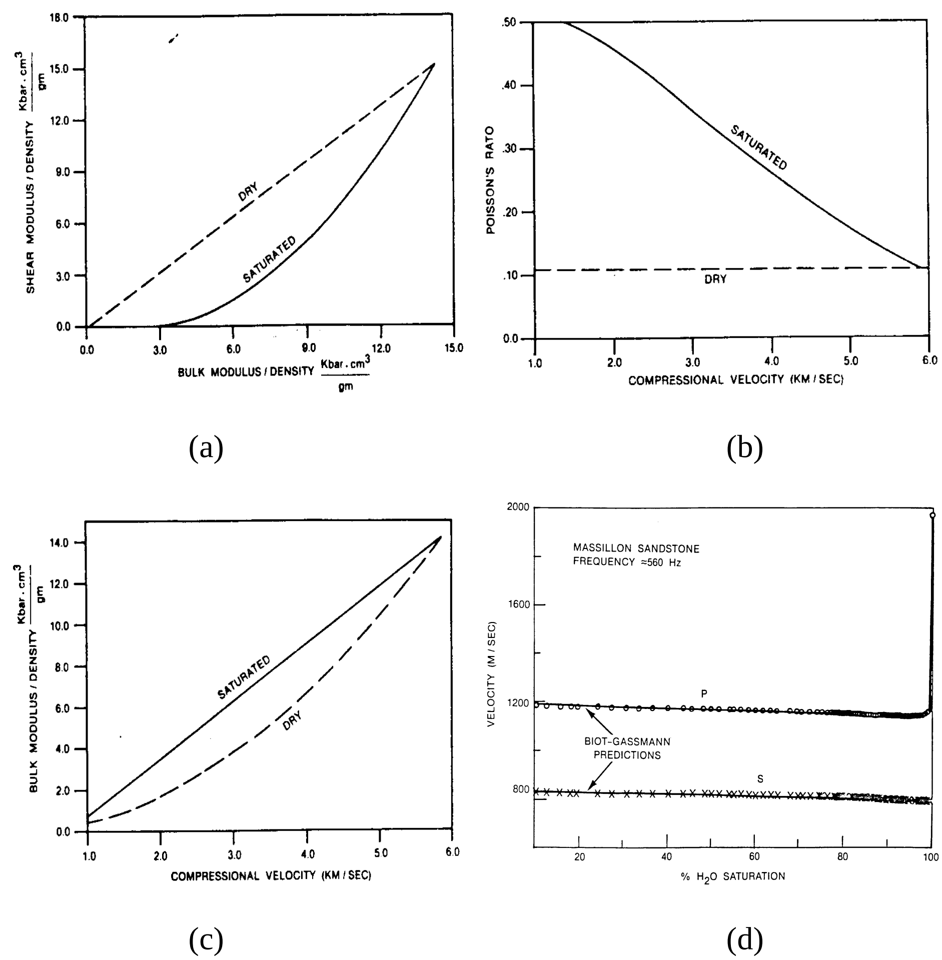

Figure 10. Relationships of clastic rocks (Castagna, 1985). (a) The computed relationships between the bulk and shear moduli (normalized by density) based on the observed Vs and Vp trends. (b) The computed relationships between Poisson's ratio and Vp based on the observed Vs and Vp trends. (c) The computed relationships between the bulk modulus (normalized by density) and Vp based on the observed Vs and Vp trends. (d) Gassmann's equation prediction and observed Vp and Vs.

κ–μ as direct hydrocarbon indicator

Compared with the grain bulk modulus and frame bulk modulus, the bulk modulus of gas is small enough to be ignored, the *Q* in equation (17b) is approximated to zero. That means the gas-saturated rock behaves as dry rock. So (κ–μ) is close to zero for gas sand. In Figure 10 (a), there are always big differences between bulk moduli of water-saturated rock and dry rock when Vp < 6km/s. Therefore (κ–μ) should be very sensitive to the gas existing. In addition, the partially water-saturated rocks behave as dry rocks. The Gassmann equation and laboratory results in Figure 10 (d) support this point.

Figure 11, Figure 12 and Figure 13 are crossplots of elastic parameters for some rock samples, which are used by Goodway et al (1997). Figure 11 shows the crossplot of incompressibility ($\lambda\rho$) and shear modulus ($\mu\rho$), and it is the result from

Goodway et al (1997). The threshold cutoff for porous gas sand is shown. In Figure 12, the bulk modulus (κρ) and shear modulus (μρ) are cross-plotted. We note that the gas sand samples are around the dry rock line. Even the shaly gas sand samples are close to the dry rock line. In Figure 13, ((κ–μ)ρ) and (μρ) are cross-plotted. The threshold cutoff for porous gas sand is easy to be determined. It is the (κ–μ=0) line. The gas sand and shaly gas sand gather around this line. In Figure 11, Figure 12, and Figure 13, the carbonate samples are all easy to be separated from shale and sand samples.

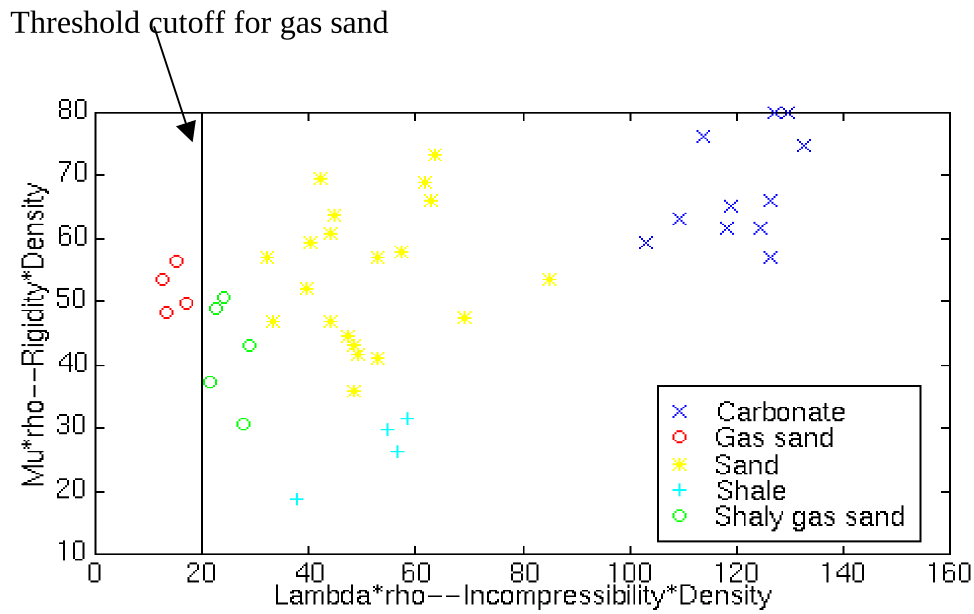

Figure 11. λρ vs μρ crossplot of Gas well log data (Goodway et al, 1997)

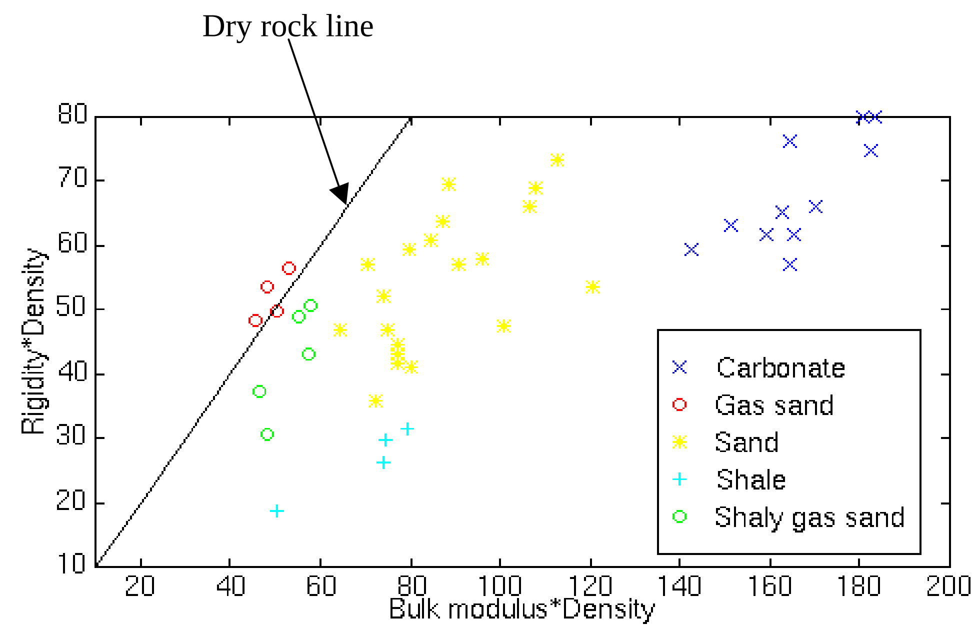

Figure 12**.** κρ vs μρ crossplot of Gas well log data.

As gas causes κ in wet rock to change significantly, and μ does not change as gas fills the dry rock frame, we consider the sensitivity of ($\kappa-\mu$) to detect the gas existing in rocks. The Table 2 gives various rock property values, from the young gas log data used by Goodway et al (1997), and average % change i.e. contrast at the interface for detectability As $\kappa=\lambda+2/3\mu$, κ is not as sensitive to detect fluid as λ because the sensitivity is diluted by $2/3\mu$ (i.e. non-pore fluid). However, the $(\kappa-\mu)=(\lambda-1/3\mu)$ is more sensitive than λ to detect the gas existing. And quantitatively, ($\kappa-\mu$) is round zero with gas in the rock. In Table 2 actual Vp, Vs, and ρ values from a shallow well have been combined to give various rock property values. Except κ, $\kappa-\mu$, $(\kappa-\mu)/\mu$ (bold), all other values are quoted from Goodway's paper. By comparing the average percentage changes of λ and $\kappa-\mu$, we note $\kappa-\mu$ is more sensitive than λ to variations in rock properties going from capping shale to gas sand. And the average % change of $(\kappa-\mu)/\mu$ ratio is greater than the average % change of λ/μ.

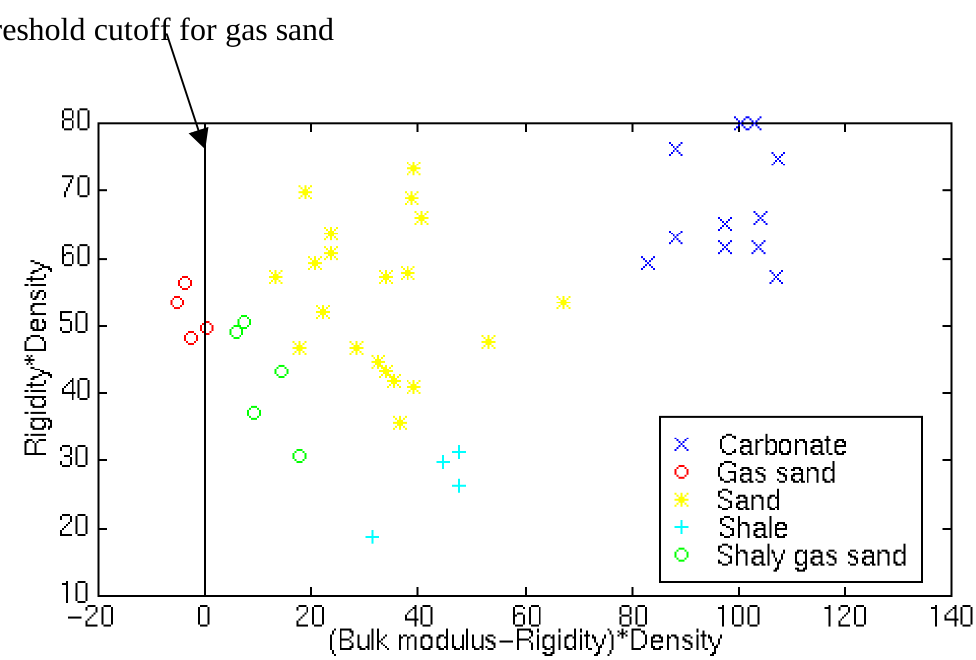

Figure 13. $(\kappa-\mu)\rho$ vs $\mu\rho$ crossplot of Gas well log data.

	Vs	Vp	ρ
Shale	1290	2898	2.425
Gas Sand	1666	2857	2.275

$\Delta Vs/Vs=0.25$ $\Delta Vp/Vp=-0.014$ $\Delta\rho/\rho= -0.064$

	Vp/Vs	$(Vp/Vs)^2$	σ	$\lambda+2\mu$	λ	μ	κ	λ/μ	$\kappa-\mu$	$(\kappa-\mu)/\mu$
Shale	2.25	5.1	0.38	20.37	12.3	4.035	15.0	3.1	11.0	2.73
Gas sand	1.71	2.9	0.24	18.53	5.9	6.314	10.1	0.9	3.8	0.60
Avg. %change	27	55	45	9.2	70	44	**39**	110	**97**	**128**

Table 2. Shallow Gas Sand Log Measurements (Goodway et al, 1997)

Crossplots of elastic parameters in Blackfoot

Figure 14 shows cross-plots of the attributes of well 08-08 in Blackfoot survey. (a) shows p velocity, s velocity and density. (b) is the crossplot of p-velocity and velocity. The linear regression is made and the line in (b) shows the fitting results. The Vp and Vs statistical relationship is Vp=1151+1.33Vs. (c) is the crossplot of p-velocity and density. The relationship between p-velocity and density is obtained by fitting: $\rho=0.25Vp^{0.27}$. (d) is the crossplot of s-velocity and p-velocity showing the channel sand in the circle. (e) is the crossplot of shear modulus (μ) and bulk modulus.(κ). (f) is the crossplot of incompressibility (λ) and shear modulus (μ). (g) is the crossplot of shear modulus (μ) and ($\lambda+2\mu$). (h) is the crossplot of shear modulus (μ) and ($\kappa-\mu$). The channel sand samples are in the circles. We note that in (e) the channel sand samples are close to the dry line and in (f) and (h) the samples outside the channel are more scattered, and in (h), the ($\kappa-\mu$) of channel sand samples are close to threshold cutoff for gas existing.

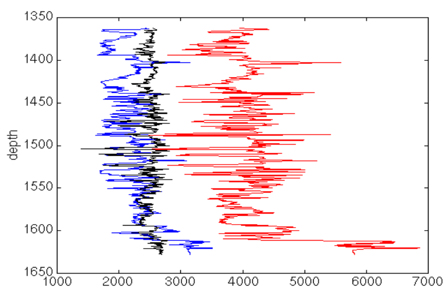

(a)

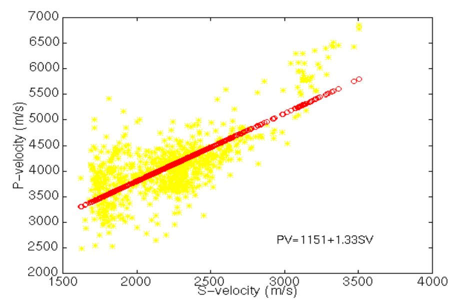

(b)

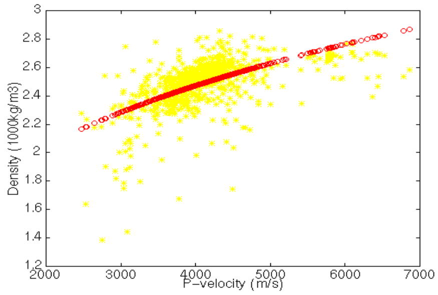

(c)

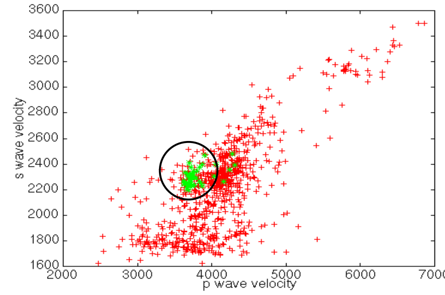

(d)

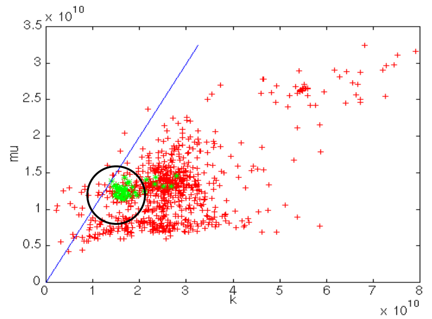

(e)

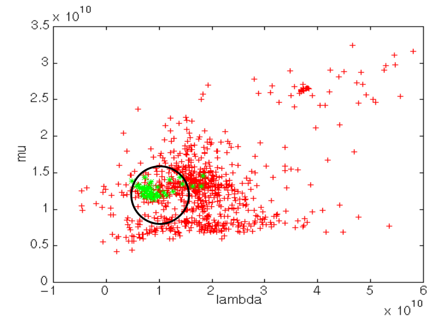

(f)

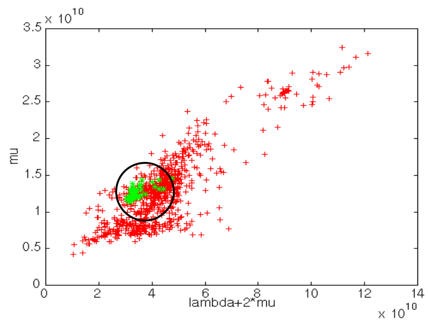

(g)

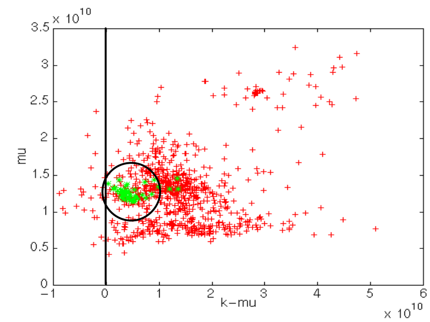

(h)

Figure 14. Cross-plots of well 08-08 in Blackfoot

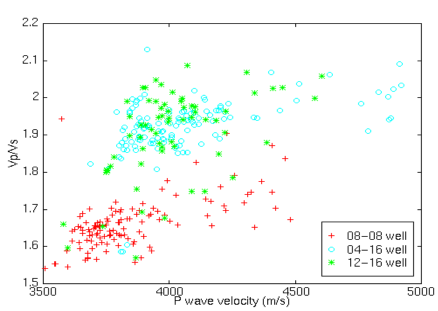

(a)

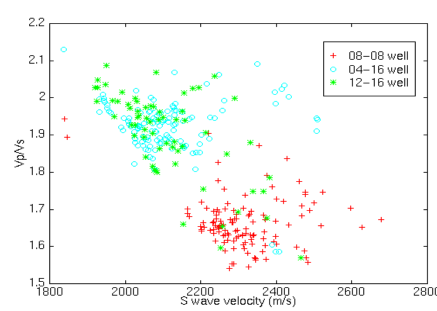

(b)

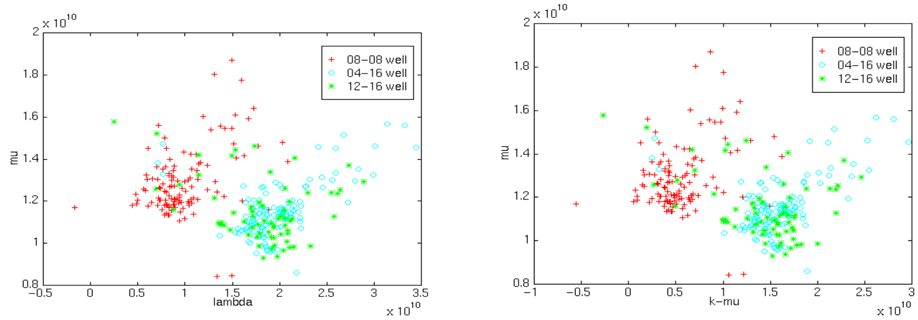

(c) (d)

Figure 15. The cross-plots of elastic parameters of the Glauconitic formation

In Figure 15, elastic parameters of Glauconitic formation in Blackfoot are cross-plotted. Rock samples from three wells are used from top to base of Glauconitic formation. The samples of Well 0808 are far away enough from samples of other wells on each crossplot to be separated from each other.

AMPLITUDE PRESERVING PROCESSING

The data applied to AVO analysis are expected to preserve relative amplitude information for all offsets at all times for any amplitude among all depth. The process of CDP stacking cancels many types of noise, and in the prestack domain where AVO used, various types of noise that distort the true amplitudes of the seismic data have to be removed by different noise suppression processes. Dey-Sarkar and Svatek (1993) defined three basic types of noise that distort the amplitudes in the prestack domain; here we quote their definition.

Type I noise phenomena can be removed without any prior knowledge of subsurface velocities and densities. These phenomena are:

(a) source generated noise,

(b) multiples,

(c) surface-consistent source-receiver effects, and

(d) source signature variation with offset.

Usual techniques to remove these effects are (1) 2D Fourier techniques; and (2) surface-consistent computation.

Type II noise is generally associated with instrumentation or cultural noise during data acquisition. Some examples are

(a) High-frequency noise,

(b) Low-frequency noise,

(c) Drilling noise, and

(d) Channel imbalance problems.

Type III noises are entirely due to wave propagation effects in a visco-elastic medium. They are

(a) 2D spherical divergence,

(b) thin bed attenuation,

(c) array attenuation,

(d) inelastic attenuation,

(e) curvature effects, and

(f) overburden transmission effects.

In general, wave propagation phenomena have a tendency to reduce the amplitude in the far offsets relative to near offsets. The trouble with this type of deterministic correction is two-fold:

(1) The knowledge of subsurface parameters necessary to compute the amplitude corrections is often inadequate and sometimes nonexistent.

(2) The 2D inhomogeneity causes rapid variation of these parameters, thus making the deterministic corrections unreliable outside the point of control.

An approach advocated by Dey-Sarkar and Svatek (1993) is to calibrate the amplitudes using some statistical procedure. After the Type I and Type II noises are removed from the prestack data, there are two components of the amplitude. The first component is associated with the amplitude variation due to Type III noise. The second component is associated with the reflection coefficient variation with offset. We would like to extract the second component and remove the first component. This cannot be achieved by analyzing an event of interest, which is contaminated by the reflection coefficient variation. We estimate the first component (Type III noise) from a window of events above the target event. The rms amplitudes are computed for each offset and an exponential decay function is fitted through the data points. The coefficient of this decay function is the amplitude correction factor for the event. The coefficient is spatially averaged to obtain a smoothly varying function. The advantages of this technique are, (1) the robustness, (2) no subsurface parameters are assumed, and (3) no distortion is produced in the data because of the slowly varying function. In this paper, we choose difference time window and CDP location to calculate the correction factors and interpolate these sparse factors to obtain correction factor for each time and CDP location. The final correction factors are time and laterally various. Figure 17 is an example using above technique. Panel (b) is the amplitude preserved processing result from panel (a). Panel (c) is the synthetic gather from the well log nearby. The left most trace in each panel is the stack trace from panel (a). Compared with gather on Panel (a), the gather on Panel (b) is improved.

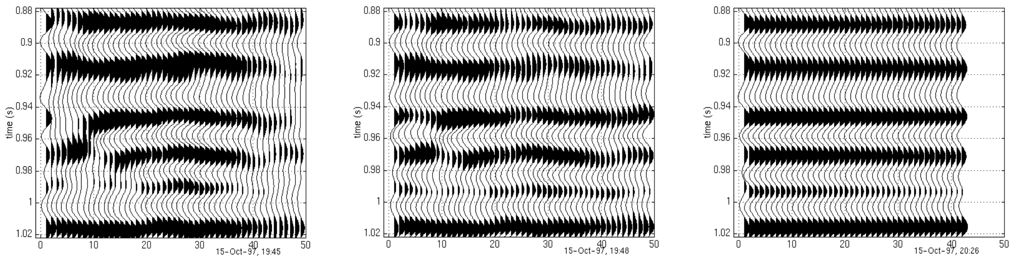

(a) (b) (c)

Figure 17. (a) the gather before amplitude calibration. (b) the gather after amplitude calibration. (c) the synthetic gather.

EXTRACTIONS OF ELASTIC PARAMETERS FROM BLACKFOOT 10 HZ VERTICAL DATA

Least square regression analysis and inversion are the common approaches in the AVO analysis. Parson (1986) obtained contrasts of three elastic parameters (λ, μ, and ρ) by pre-stack inversion. Goodway et al (1997) obtained the Vp and Vs from inversion and converted them to the λ/μ to detect the reservoirs. However, the nonuniqueness is always the problem in the seismic inversion. The background velocity error causes the ratio change greatly or eliminates the high frequency contrast. Appropriate selection of parameters, background velocity, wavelet estimation, application of a priori information are still important issues which remain to be resolved. Here we choose the least square regression analysis to extract elastic parameters from pre-stack data. The extraction provides band-limited information. And we also invert the band-limited result by recursive inversion and model-based inversion. In the regression analysis, we express the P-P and P-S reflection coefficient equations with the elastic parameters (λ and μ, or κ and μ) and extract these parameters directly without conversion from velocity.

Expressing reflection coefficients with elastic parameters

Some authors pointed out the need for a more physical insight afforded by elastic parameters (Castagna et al. 1993, Stewart 1995, Goodway et al 1997) in the approximation of reflection coefficients. Castagna (1993) also indicated the bulk modulus that is embedded in Vp links velocity with rock properties for pore fluid detection. So we may benefit from the conversion from velocity measurements to modulus parameters of rigidity (μ), bulk modulus (κ), incompressibility (λ).

Aki-Richards' reflection coefficient formula for P-P reflection can be rewritten as the combination of contrasts of incompressibility (λ), shear modulus (μ), and density (ρ) (Parson 1986, Goodway et al. 1997) as follows:

$$PP = \frac{1}{4}(1+\tan^2 i)\frac{\Delta(\lambda+2\mu)}{(\lambda+2\mu)} - 2(\frac{Vs}{Vp})^2 \sin^2 i\frac{\Delta\mu}{\mu} + \frac{1}{4}(1-\tan^2 i)\frac{\Delta\rho}{\rho} \qquad (21)$$

Goodway et al. (1997) thought this equation not practical for AVO analysis and modified it as the impedance contrasts as equation (22). The third term in equation (22) can be cancelled with the approximations of Vp/Vs>2 and tan*i*~sin*i*. After inverting the seismic data to Vp and Vs information and using the moduli to impedance relationships to obtain the $\lambda\rho$ and $\mu\rho$, the ratio of λ/μ may be obtained. The advantages of this scheme used by Goodway et al (1997) are less unknowns and more robustness in the AVO analysis, but the low frequency information of impedance is usually not accurate from inversions which influences ratio of λ/μ the detectability of anomalies.

$$PP = (1+\tan^2 i)\frac{\Delta Ip}{Ip} - 8(\frac{Vs}{Vp})^2 \sin^2 i\frac{\Delta Is}{Is} - [\frac{1}{2}\tan^2 i - 2(\frac{Vs}{Vp})^2 \sin^2 i]\frac{\Delta\rho}{\rho} \qquad (22)$$

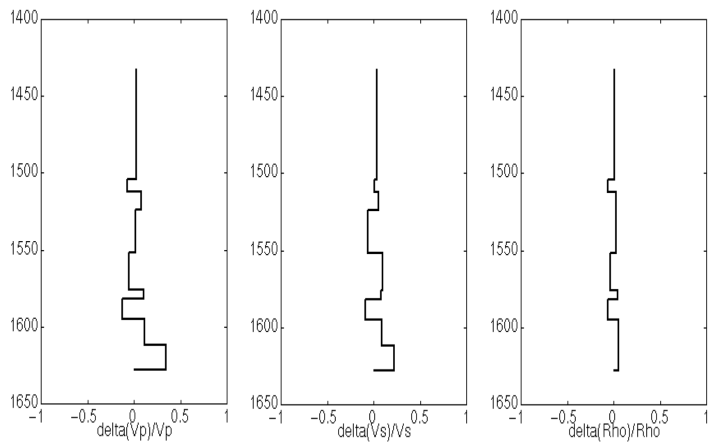

(a) (b) (c)

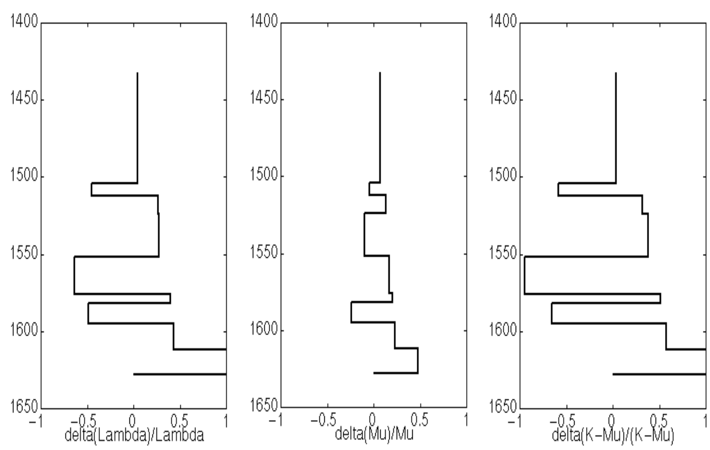

(d) (e) (f)

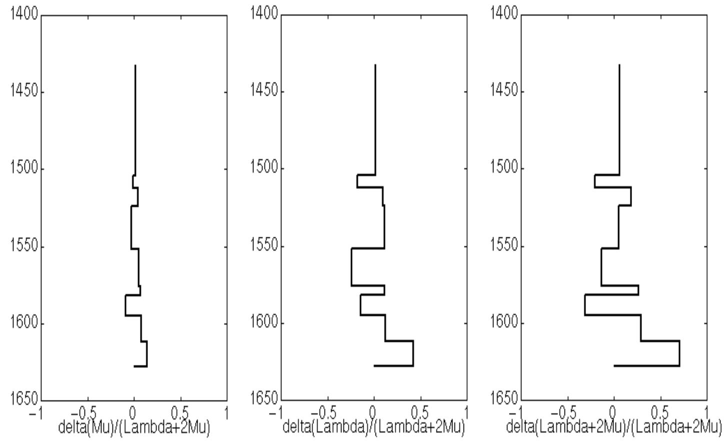

(g) (h) (i)

Figure 18. Comparisons of various relative changes of rock parameters from well 08-08 in Blackfoot survey. (a) $\Delta Vp/Vp$; (b) $\Delta Vs/Vs$; (c) $\Delta\rho/\rho$; (d) $\Delta\lambda/\lambda$; (e) $\Delta\mu/\mu$; (f) $\Delta(\kappa-\mu)/(\kappa-\mu)$; (g) $\Delta\mu/(\lambda+2\mu)$;(h) $\Delta\lambda/(\lambda+2\mu)$; (i) $\Delta(\lambda+2\mu)/(\lambda+2\mu)$.

Usually the density is the least changed parameter among density, moduli, and velocities. The normalized density changes are much smaller than modulus changes. This can be tested by well log data. The Figure 18 plots the comparisons of various relative changes of rock parameters of well 08-08 blocked model in Blackfoot survey. Note the small relative change of density compared with several forms of relative changes of λ and μ. Actually the relative changes of λ and μ magnify the changes of Vp and Vs. We also notice the great change of $\Delta\mu/\mu$ at the oil bearing layer (1580 meter) and we hope the apparent change of $\Delta\mu/\mu$ on the top of this layer can be shown on the extraction results of P-S data.

Now we rewrite equation (22) to make the $(Vs/Vp)^2$ implicit.

$$PP = \frac{1}{4}(1+\tan^2 i)\frac{\Delta(\lambda+2\mu)}{(\lambda+2\mu)} - \sin^2 i\,\frac{\Delta 2\mu}{(\lambda+2\mu)} + \frac{1}{4}(1-\tan^2 i)\frac{\Delta\rho}{\rho} \tag{23}$$

It can be rewritten as the combination of contrasts of bulk modulus, shear modulus, and density as follows:

$$PP = \frac{1}{4}(1+\tan^2 i)\frac{\Delta(\kappa+\frac{4}{3}\mu)}{(\kappa+\frac{4}{3}\mu)} - \sin^2 i\,\frac{\Delta 2\mu}{(\kappa+\frac{4}{3}\mu)} + \frac{1}{4}(1-\tan^2 i)\frac{\Delta\rho}{\rho} \tag{24}$$

To make the AVO analysis more robust the third term may be neglected as the density changes are small.

$$PP \approx \frac{1}{4}(1+\tan^2 i)\frac{\Delta(\lambda+2\mu)}{(\lambda+2\mu)} - \sin^2 i \frac{\Delta 2\mu}{(\lambda+2\mu)} \tag{25}$$

Another way to make equation (24) two-term expression is to incorporate the third term into the first term. Gardner's relationship is fit to a very wide range of velocities and porosities. Gardner's relationship between density and P wave velocity is

$$\rho = aV_P{}^b \ (b\text{=}0.25), \tag{26}$$

And the relationship between moduli, density and P wave velocity is

$$V_P = \sqrt{\frac{\lambda+2\mu}{\rho}}, \tag{27}$$

From equation (26) and equation (27), an approximation of equation (24) is obtained as:

$$PP \approx \frac{1}{4}(\frac{10}{9}+\frac{8}{9}\tan^2 i)\frac{\Delta(\lambda+2\mu)}{(\lambda+2\mu)} - \sin^2 i \frac{\Delta 2\mu}{(\lambda+2\mu)} \tag{28}$$

or

$$PP \approx \frac{1}{4}(\frac{10}{9}+\frac{8}{9}\tan^2 i)\frac{\Delta\lambda}{(\lambda+2\mu)} + \frac{1}{2}(\frac{10}{9}+\frac{8}{9}\tan^2 i - 4\sin^2 i)\frac{\Delta\mu}{(\lambda+2\mu)} \tag{28'}$$

P-S reflection coefficient can also be simplified and associated with rock properties. Aki-Richards approximation for P-S reflection coefficient can be reformulated in terms of rigidity and density as:

$$PS = -\frac{1}{2}\frac{\alpha}{\beta}\tan j[\frac{\Delta\rho}{\rho} + 2\frac{\beta}{\alpha}\frac{\Delta\mu}{\mu}\cos(i+j)] \tag{29}$$

$$PS = -\frac{1}{2}\frac{\alpha}{\beta}\tan j[(\frac{\Delta\rho}{\rho} + 2\frac{\beta}{\alpha}\frac{\Delta\mu}{\mu}) - \frac{\beta}{\alpha}\frac{\Delta\mu}{\mu}(\frac{\alpha}{\beta}+1)^2 \sin^2 j] \tag{30}$$

In fact the equation (29) reveals the AVO variation for shear modulus and ρ term. The slope of P-S wave AVO is primarily dependent on the shear modulus.

As $\frac{\beta}{\alpha} \sim \frac{1}{2}$,

$$PS \approx -\tan j[\frac{\Delta\rho}{\rho} + \frac{\Delta\mu}{\mu}\cos(i+j)] \tag{31}$$

$$PS \approx -\tan j[-4R_{SS} - \frac{9}{2}\frac{\Delta\mu}{\mu}\sin^2 j] \tag{32}$$

where $R_{ss} = -\frac{1}{2}(\frac{\Delta\rho}{\rho} + \frac{\Delta\beta}{\beta})$ is the reflectivity of the normal incidence of the SH wave.

AVO analysis of P-S data

In theory, equation (31) and equation (32) can be applied to AVO analysis to get the density and rigidity relative differences if the incident angles and reflection angles are known. However, the incident P wave path and converted S wave path even in the horizontal homogeneous media are not symmetrical like the incident P wave path and reflected P wave path. It is not easy to obtain the incident angles or reflection angles for the P-S reflection and the Vp/Vs ratio is necessary even for the single interface case. In addition, the seismic data are usually sorted in common mid-point (CMP) gather form, and the conversion from CMP gather to common converted point (CCP) gather is the usual process in the P-S seismic data processing.

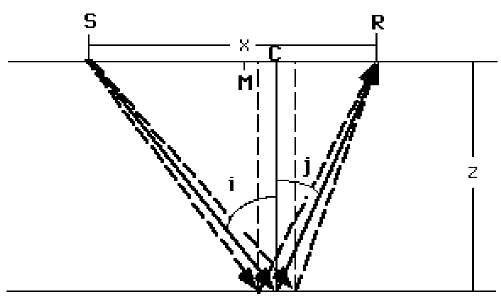

Figure 19. Illustration of propagation of incidence and converted wave.

Figure 19 illustrates the moving of converted point as the Vp/Vs ratio changes given fixed source and receiver positions. In the extraction of AVO, Vp/Vs ratio is usually approximated to a constant such as 2.0 . Now we check the influence of varying Vp/Vs ratio on the incident and converted angles. In Figure 20 the cos(i+j) in equation (31) is plotted with variation versus offsets and Vp/Vs ratios. And in Figure 21 the sin(i) is plotted with variation versus offsets and Vp/Vs ratios. And also in Figure 22 the sin(j) is plotted with variation versus offsets and Vp/Vs ratios. Two points are observed on these three figures.

sin(i) slowly varies as Vp/Vs ratio varies; and sin(j) varies as Vp/Vs ratio varies; These two kinds of changes cancel each other to make the cos(i+j) change slowly with variation of Vp/Vs ratio.

There should be smaller error to use the cos(i+j) than $\sin^2 j$ under the assumption of constant Vp/Vs. Therefore it is better to use sin(i) or cos(i+j) to AVO analysis instead of sin(j). The equation (32) can be expressed as the function of sin(i) as follow.

$$PS \approx A\sin i + B\sin^3 i \tag{33}$$

where

$$A = -\frac{1}{2}\left(\frac{\Delta\rho}{\rho} + 2\frac{\beta}{\alpha}\frac{\Delta\mu}{\mu}\right) \tag{34}$$

$$B = -\frac{1}{2}\frac{\beta^2}{\alpha^2}\left[\frac{1}{2}\frac{\Delta\rho}{\rho} - \left(\frac{\alpha}{\beta} + 2\right)\frac{\Delta\mu}{\mu}\right] \tag{35}$$

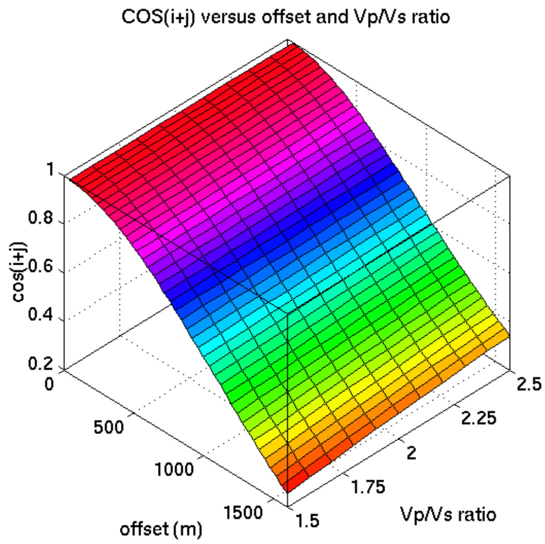

Figure 20. cos(i+j) versus offsets (40m - 1600m) and Vp/Vs ratios (1.5 - 2.5).

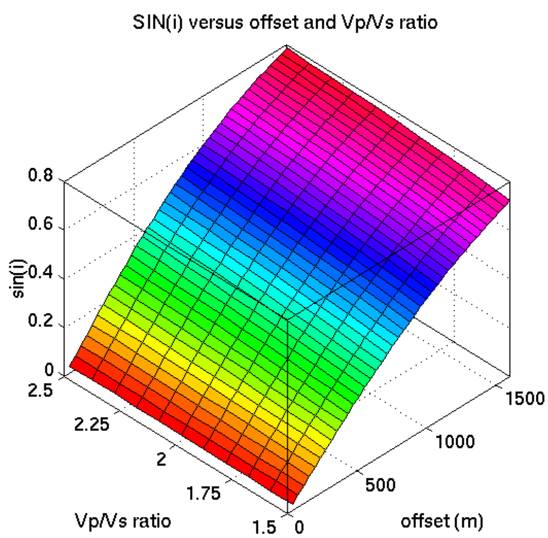

Figure 21. sin(i) versus offsets (40m - 1600m) and Vp/Vs ratios (1.5 - 2.5).

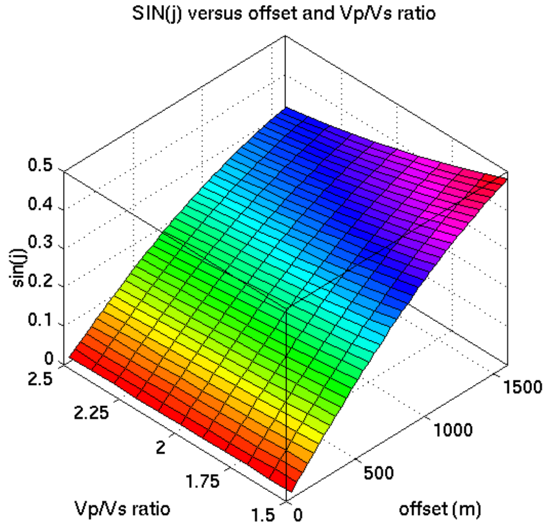

Figure 22. sin(j) versus offsets (40m - 1600m) and Vp/Vs ratios (1.5 - 2.5).

The AVO weighted stack was first mentioned by Smith and Gidlow (1987) It is in fact the least squared linear regression analysis. Ferguson (1996) inverted the Blackfoot 3C data by the weighted stack technique. The P velocity and S velocity were obtained by band-limited inversion and the Vp/Vs ratio was obtained from the inverted P and S velocity information. Here we hope to apply another scheme to extract the elastic parameter from the P-S data. From equation (31), the least square regression can be employed to extract the contrasts of density and shear modulus. We hope to get the relative reliable density contrast from the extraction. And also the contrast of shear modulus can test the extraction result from P-P data. Because of the more difficulties to process radial component data set to obtain the preserved amplitude, good aligned events, and corrected incident and reflected angles, efforts are still making on the Blackfoot data sets and reasonable results will be shown in near future.

Elastic parameter extraction from Blackfoot 10 Hz vertical

Pre-stack seismic data were acquired from 10 Hz Blackfoot seismic data set, with preliminary processing and amplitude-preserving processing applied.

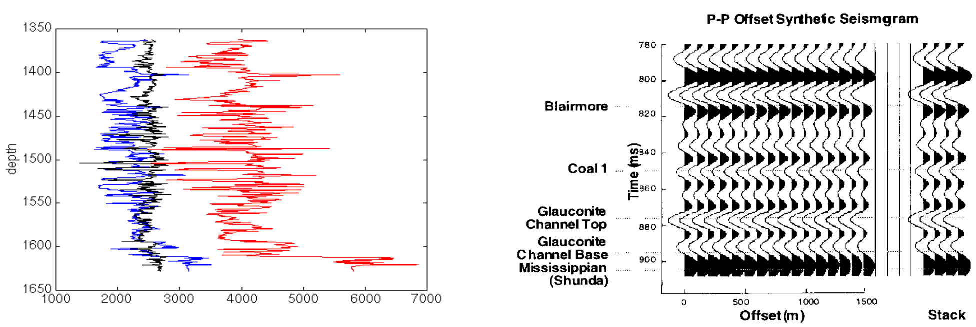

(a) (b)

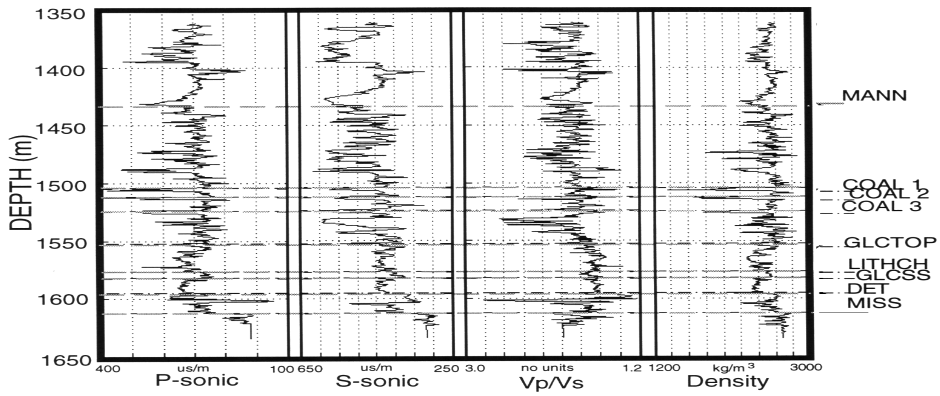

(c)

Figure 23 Well 0808 and synthetic gather from the well

Figure 23 are the well logs of well 0808 and the synthetic gather (Margrave et al, 1995, Potter et al, 1996). The Glauconitic channel formation is shown on the well logs. From the P-wave velocity and density contrasts, the channel sand is Class III sand (Rutherford and Williams, 1989) with low P impedance in sand. However the impedance changes is not much, and on the synthetic gather the AVO anomaly is not significant.

Using equation (28), the relative contrasts, $\frac{\Delta(\lambda+2\mu)}{\lambda+2\mu}$ and $\frac{\Delta\mu}{\lambda+2\mu}$ are obtained by linear regression. By combining these contrasts, the contrasts of $\frac{\Delta\lambda}{\lambda+2\mu}, \frac{\Delta(\kappa-\mu)}{\lambda+2\mu}$ and $\frac{\Delta\gamma}{\gamma}$ are also derived,

where $\gamma = \alpha/\beta$ is the Vp/Vs ratio and

$$\frac{\Delta\gamma}{\gamma} = \frac{1}{2}\left(\frac{\Delta\lambda}{\lambda+2\mu} - \frac{(\gamma^2-2)\Delta\mu}{\lambda+2\mu}\right) \approx \frac{1}{2}\left(\frac{\Delta\lambda}{\lambda+2\mu} - \frac{2\Delta\mu}{\lambda+2\mu}\right)$$

Figure 24 shows the above five contrasts within the seismic frequency bandwidth (5-10-60-70 Hz).

In Figure 24 (a) the contrast of $\Delta(\lambda+2\mu)/(\lambda+2\mu)$ shows anomaly in the box (cdp 130-170, time 1000ms-1100ms) which is the approximated location of Glauconitic channel. The box shows the zone with difference from neighborhood. The extracted $\Delta\mu/(\lambda+2\mu)$ section is displayed in Figure 24 (b). In the box on Figure 24 (b), the Glauconitic channel shape can be been. But on the top and bottom and in between the $\Delta\mu/(\lambda+2\mu)$ changes continuously from the neighbor zones. Figure 24 (c) is obtained by subtraction of two times (b) from (a). It approximates $\Delta\lambda/(\lambda+2\mu)$.The anomaly shown in Figure 24 (a) can also be seen, however it is weaker than on Figure 24 (a). On figure 24 (d), the $\Delta(\kappa-\mu)/(\lambda+2\mu)$ is plotted. The channel has a white infillment, which means the less change of $(\kappa-\mu)$. One possibility is the near zero $(\kappa-\mu)$. On Figure 24 (e), the $\Delta\gamma/\gamma$ has greater change within the channel than in the neighborhood.

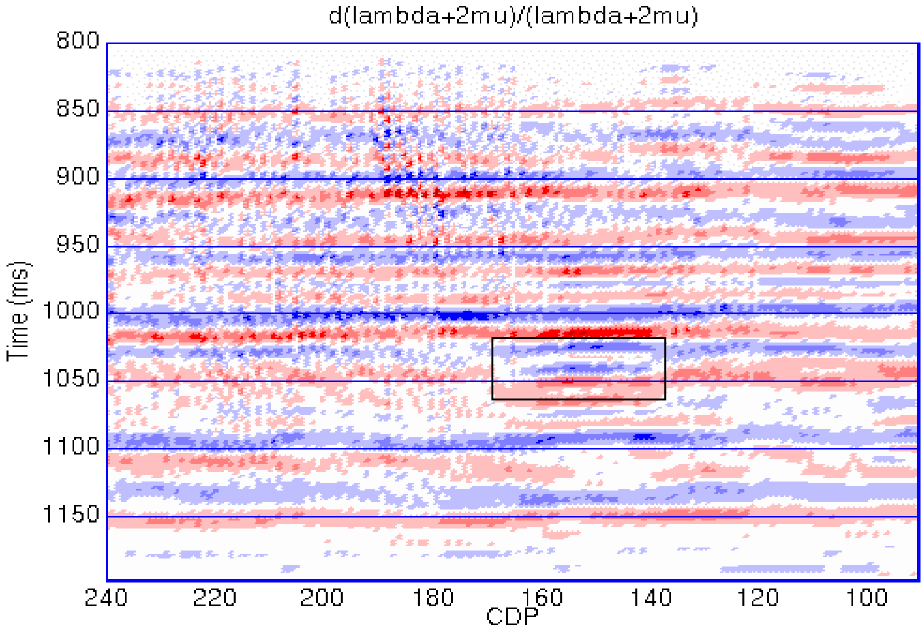

(a) the section of $\Delta(\lambda+2\mu)/(\lambda+2\mu)$

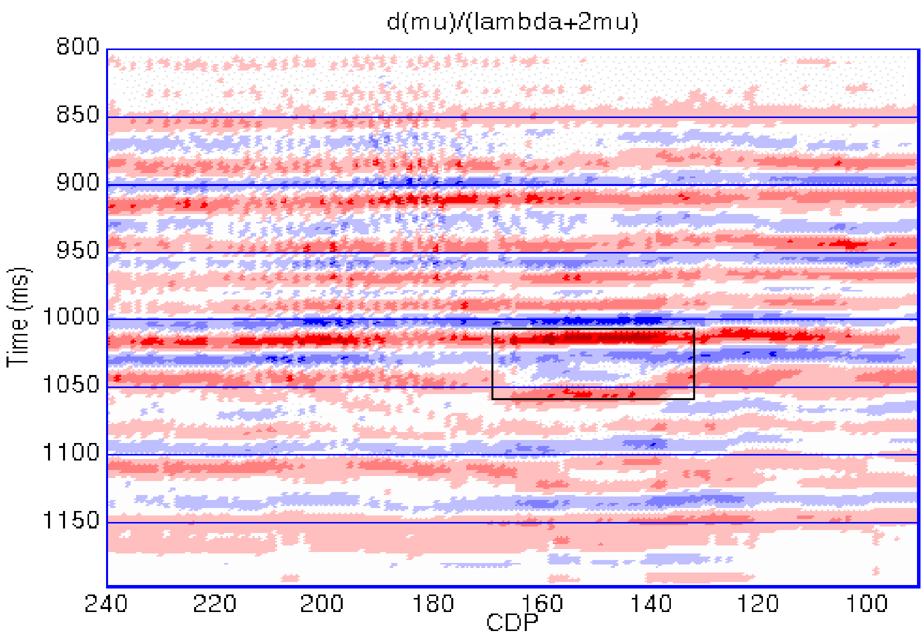

(b) section of $\Delta\mu/(\lambda+2\mu)$

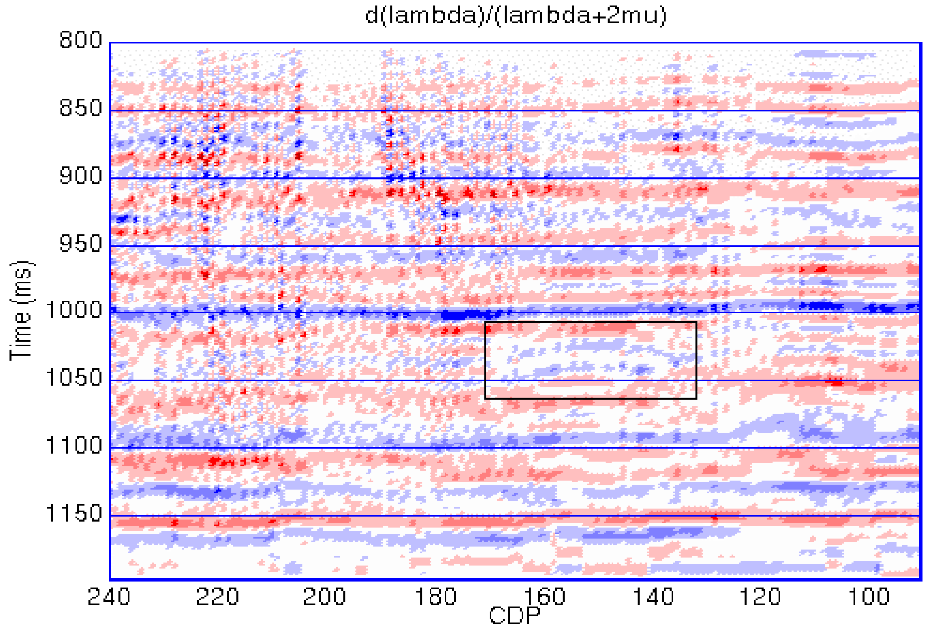

(c) the section of $\Delta\lambda/(\lambda+2\mu)$

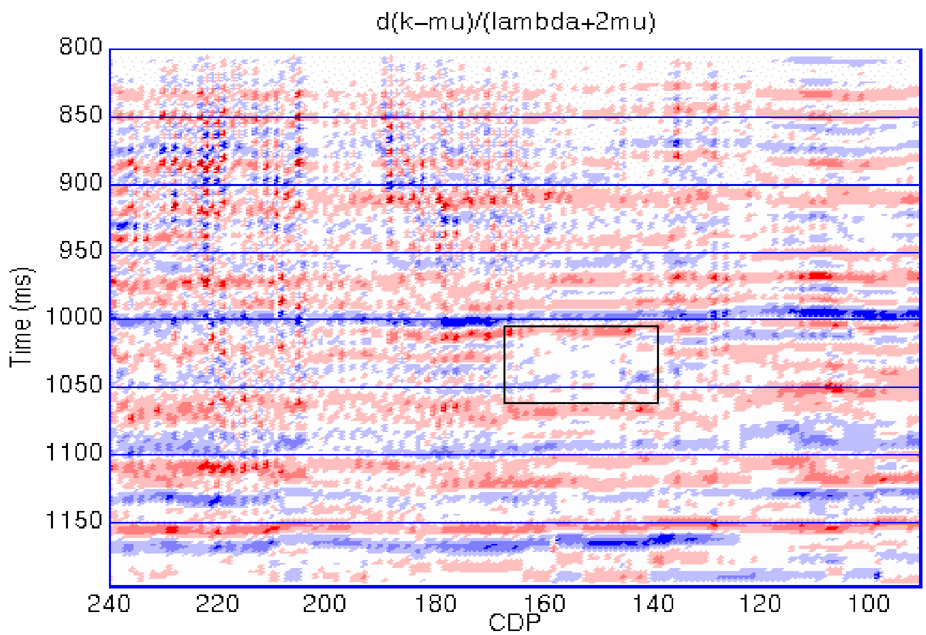

(d) the section of $\Delta(\kappa-\mu)/(\lambda+2\mu)$

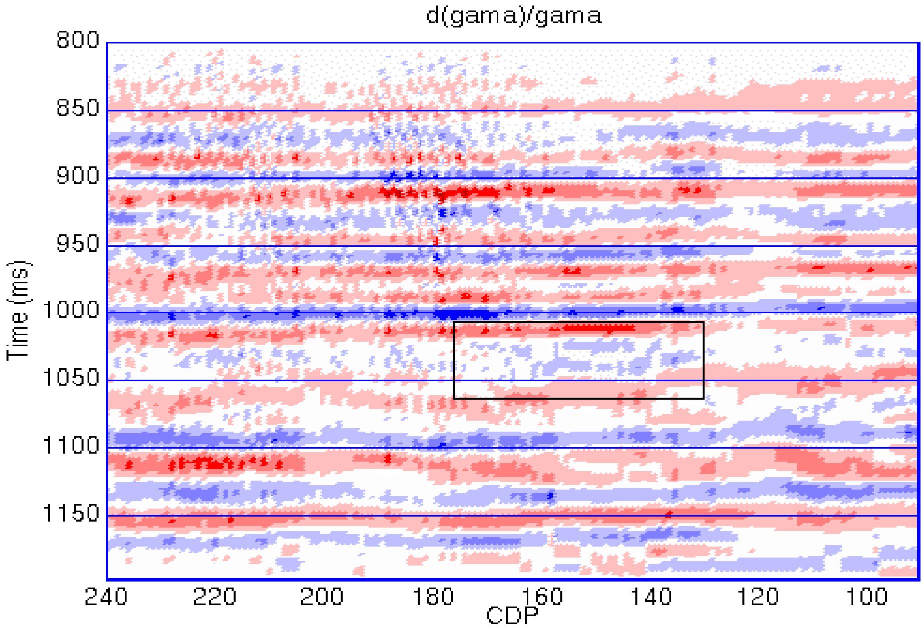

(e) the section of $\Delta\gamma/\gamma$ (γ is the Vp/Vs ratio).

Figure 24. the analysis results of Blackfoot vertical seismic data.

Figure 25 shows the inversion results from the extraction sections in figure 24. The low frequency components are obtained from the wells. The recursive integration of the AVO extraction sections in Figure 24 is merged with the low frequency components.

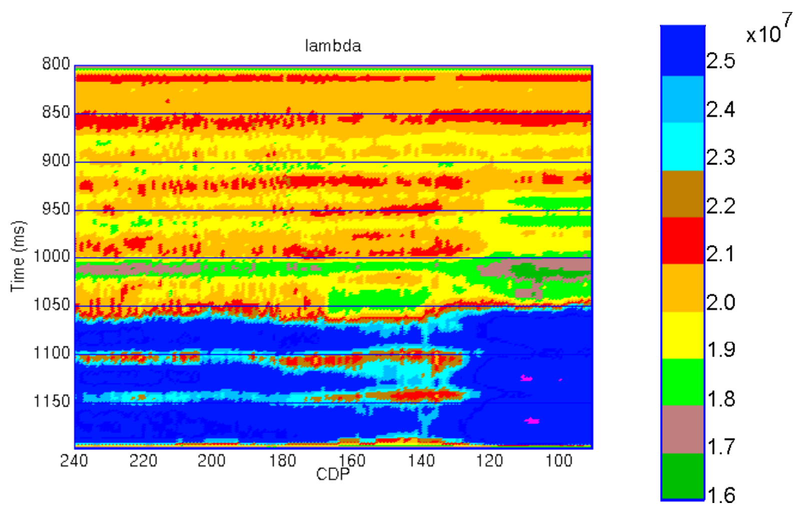

(a) λ

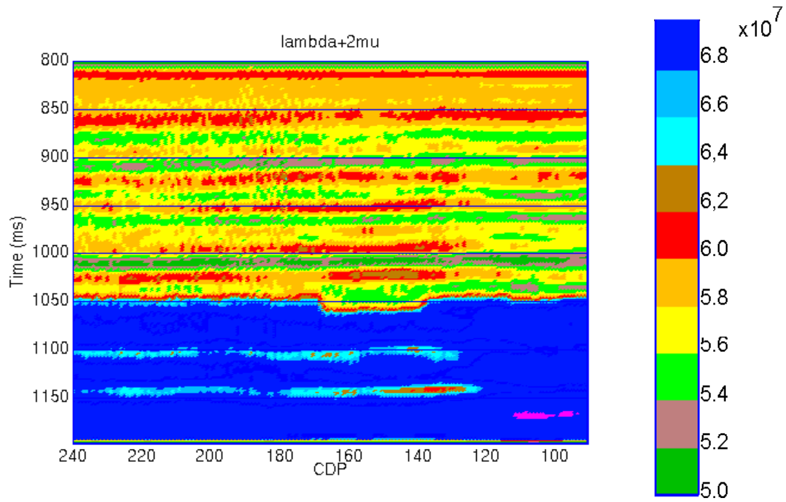

(b) $\lambda+2\mu$

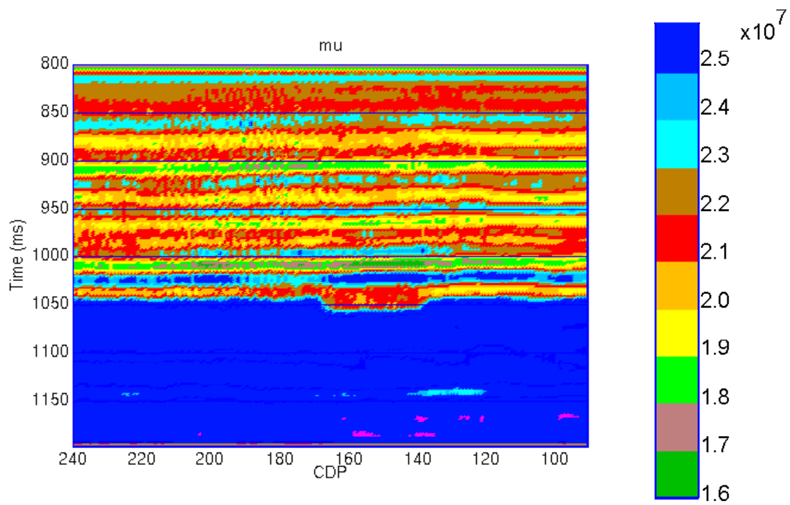

(c) μ

Figure 25. The inversion results from Figure 24.

ZERO OFFSET STACK

It is well recognized that amplitude and phase variation versus offset may cause CDP stacking to degrade reflection data quality. The extraction of the intercepts by least squares regression produces a "zero offset" stack (Denhem et al, 1985, coruh and Demirbag, 1989). On the other hand, we hope to obtain reservoir information by various approaches to overcome the limits of seismic data. The zero offset section provides (1) a better approximation to the normal incidence P-wave reflection coefficient, (2) broader bandwidth and higher frequencies, and (3) high resolution. Seismic impedance traces inverted from zero offset stack traces should be superior to from conventional seismic stack sections.

Approximation of P-P reflectivity in term of offsets

Aki-Richards approximation of P-P reflectivity can be written as

$$PP = A + B\tan^2 i + C\tan^4 i \tag{36}$$

where

$$A = \frac{1}{2}\left(\frac{\Delta\rho}{\rho} + \frac{\Delta\alpha}{\alpha}\right)$$

$$B = \frac{1}{2}\frac{\Delta\alpha}{\alpha} - 2\frac{\Delta\rho}{\rho} - 4\frac{\Delta\beta}{\beta}$$

$$C = -2\left(\frac{\Delta\rho}{\rho} + \frac{\Delta\beta}{\beta}\right)$$

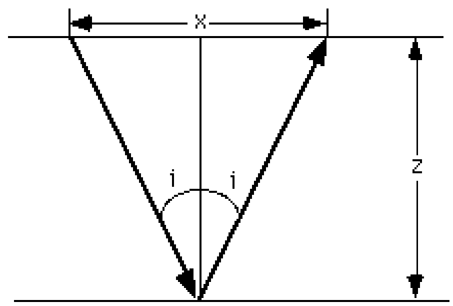

Figure 26 Reflection of compressional wave at the interface of media.

If the wave propagation path is shown as Figure 26, the P-P reflectivity can expressed as function of offsets as

$$PP = A + B'x^2 + C'x^4 \tag{37}$$

where

$$A = \frac{1}{2}\left(\frac{\Delta\rho}{\rho} + \frac{\Delta\alpha}{\alpha}\right)$$

$$B' = \left(\frac{1}{2}\frac{\Delta\alpha}{\alpha} - 2\frac{\Delta\rho}{\rho} - 4\frac{\Delta\beta}{\beta}\right)/(4z^2)$$

$$C' = -2\left(\frac{\Delta\rho}{\rho} + \frac{\Delta\beta}{\beta}\right)/(8z^4)$$

Therefore, the AVO analysis can be done by curve fitting of the offsets. And the *A* in the above equation is independent on the changes of variables of x or sin*i*. And the normal incidence reflectivity is easy to be obtained in the AVO analysis.

Even with an incident angle of 45 degrees recovery of the third term is less robust than second term recovery. Therefore another further approximation is commonly used.

$$PP = A + B'x^2 \qquad (37)'$$

AVO in F-X domain

Consider the convolutional earth model. The seismic trace is expressed as the convolution of reflectivity and wavelet as (38)

$$T(t,x) = R(t,x) * W(t) \qquad (38)$$

Where T(t) is the seismic trace, R(t) is the reflectivity, and W(t) is the wavelet.

$$R(t,x) = A(t) + B(t)\, x^2 + C(t)\, x^4$$

$$T(t,x) = A(t)*W(t) + B(t)*W(t)\, x^2 + C(t)*W(t)\, x^4$$

$$T(t,x) = P(t) + Q(t)\, x^2 + S(t)\, x^4$$

$$T(f,x) = P(f) + Q(f)\, x^2 + S(f)\, x^4 \qquad (39)$$

$$T(f,x) = P(f) + Q(f)\, x^2 \qquad (39')$$

where T = P, Q ,and S are the spectra of P, Q, and S.

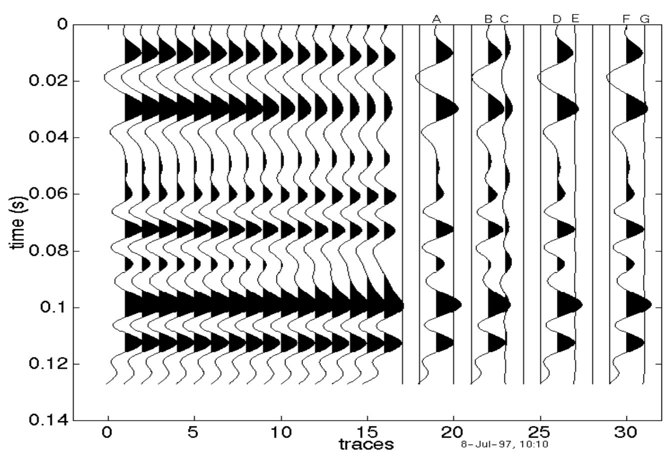

Figure 27 Comparison of normal incidence trace, stack trace, and fitting traces in time domain and frequency domain.

In Figure 27, the first 16 traces in the left are of the same CDP gather. Trace 19 labeled as ‘A’ is normal incidence trace coming from convolution of zero offset reflectivity and wavelet. Trace 22 labeled as ‘B’ is the stack trace, and trace 23 (labeled as ‘C’) is the error of stack trace. Trace 26 with label ‘D’ is the fitting trace in time domain and trace 27 with label ‘E’ is the error of trace 26. Trace 30 labeled as

'F' is the fitting trace in frequency domain and trace 31 labeled as 'G' is the error of trace 30. Here the fitting traces are using the second order approximation. The fitting traces are closer to the normal incidence trace both for the t-x domain and f-x domain.

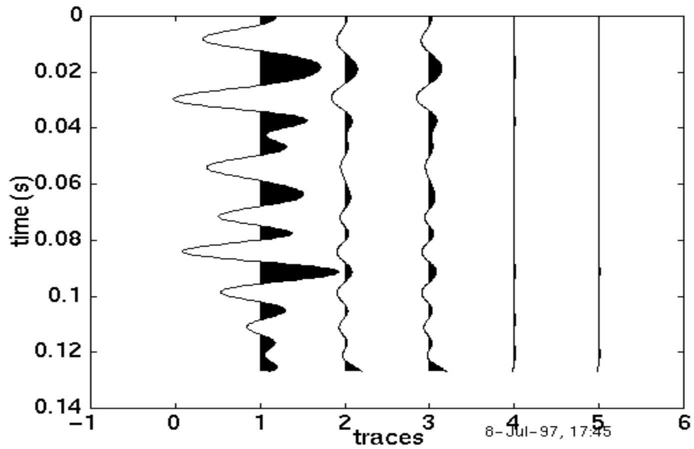

Figure 28. Comparison of errors of traces from different methods.

In Figure 28, the errors of traces from different methods are compared. Trace 1 is the error of stack trace. Trace 2 is the error of fitting trace in t-x domain by equation (37'). Trace 3 is the error of fitting trace in f-x domain by equation (39'). Trace 4 and trace 5 are the errors of fitting traces in t-x domain and f-x domain with by equation (37) and equation (39). From the comparison, three points are concluded: first, the fitting trace has smaller error than stack trace; second, the higher order approximation fitting trace has smaller error than the low higher order approximation fitting trace; and last, the results in the t-x domain and f-x domain are equivalent.

Figure 29 displays real parts (left panel) and imaginary parts (right panel) of the spectra of each trace in the CDP gather used to curve fitting. The spectrum value for frequency greater than 125 Hz is zero in this case. Therefore, the curve fitting for the big frequency band is not necessary, and the calculation is saved. That compensates the cost of fast Fourier transform. The following values compare the running times of t-x and f-x domain curving fitting.

The CDP gather has 12 traces, 128 samples, and time sample rate 0.1s. The running time in t-x domain is 0.331s and in f-x domain 0.229s.

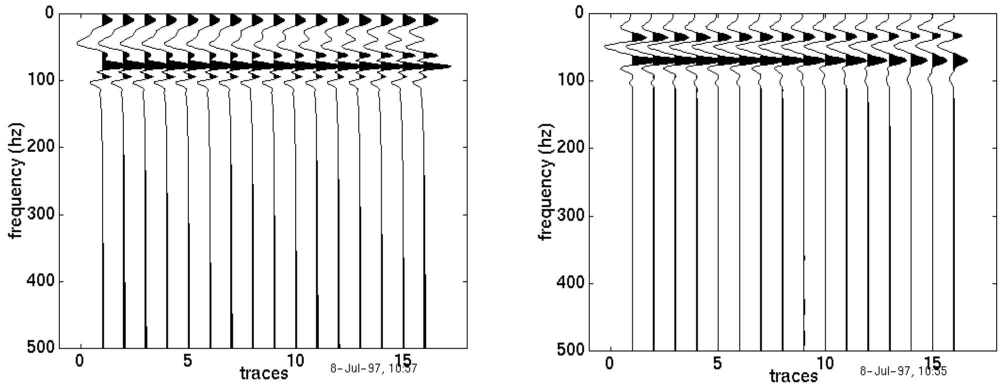

Figure 29. The real parts (left) and the imaginary parts (right) of spectra of the CDP gather.

Zero offset sections of Blackfoot survey

In Figure 30, zero offset and conventional stack sections are plotted. The seismic data are from Blackfoot 2D-3C survey. Panel (a) is the zero offset stack section and panel (b) is the conventional stack section. Offsets for the dataset are limited within 100m-2500m. The panel (c) is the zero offset stack by curve fitting in F-X domain. From comparison of these couples of sections, it can be noted that the resolution on the zero offset section is higher than the convention stack section.

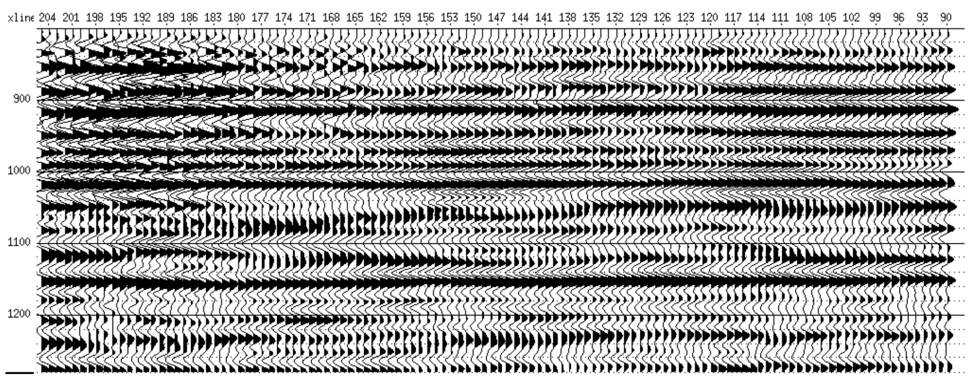

(a)

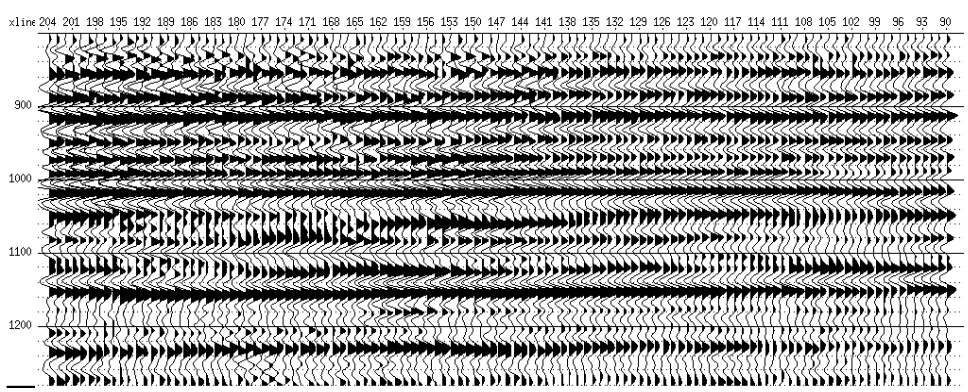

(b)

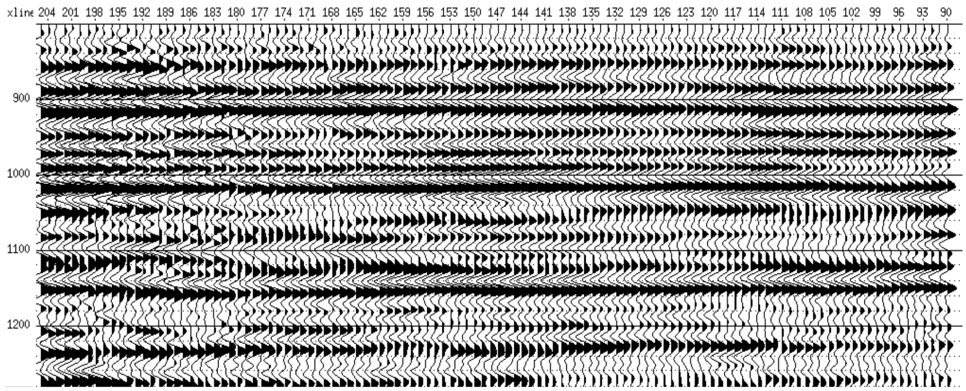

(c)

Figure 30 Comparison of zero offset stack and conventional stack

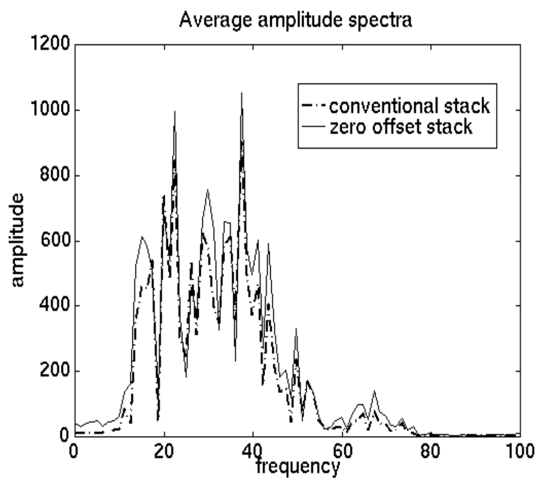

Figure 31. Amplitude spectra of zero offset stack and conventional stack.

In Figure 31 the average amplitude spectra of zero offset stack and conventional stack sections in figure 29, panel (a) and (b), are displayed. The enhanced low and high frequency component of the zero offset stack can be noticed.

The zero offset section of panel (a) in Figure 30 is used to the impedance inversion. The results are shown in Figure 32. In Figure 32, panel (a) is the interpretation result by Miller et al (1995), which is used to control the model-based inversion. Panel (b) is the inverted impedance section. Panel (c) is the enlargement of the Glauconitic channel. Panel (d) is the correlation of synthetic traces of well logs from well 08-08 and well 09-14 with seismic traces in panel (a), and panel (e) is the correlation of synthetic traces of well logs from well 08-08 and well 09-14 with conventional stack traces in panel (b) of Figure 30.

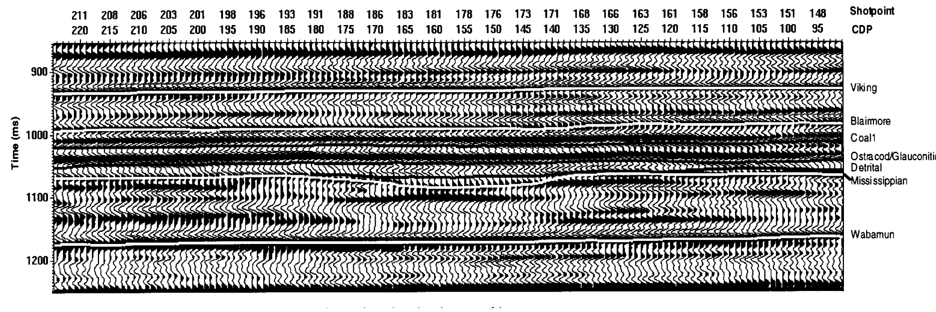
Shotpoint
CDP
Time (ms)
900
1000
1100
1200
Viking
Blairmore
Coal1
Ostracod/Glauconitic
Detrital
Mississippian
Wabamun

(a)

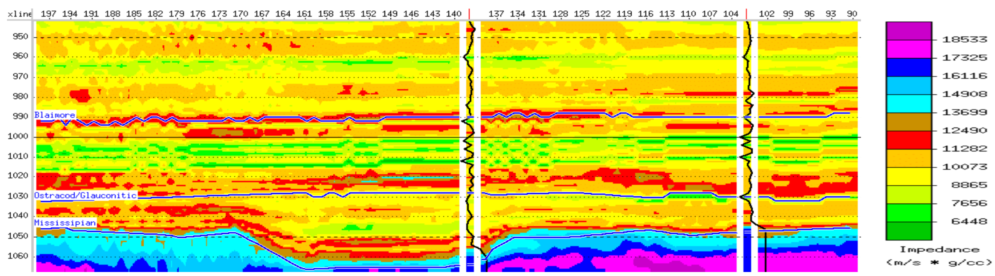
xline
Blairmore
Ostracod/Glauconitic
Mississipian
18533
17325
16116
14908
13699
12490
11282
10073
8865
7656
6448
Impedance
(m/s * g/cc)

(b)

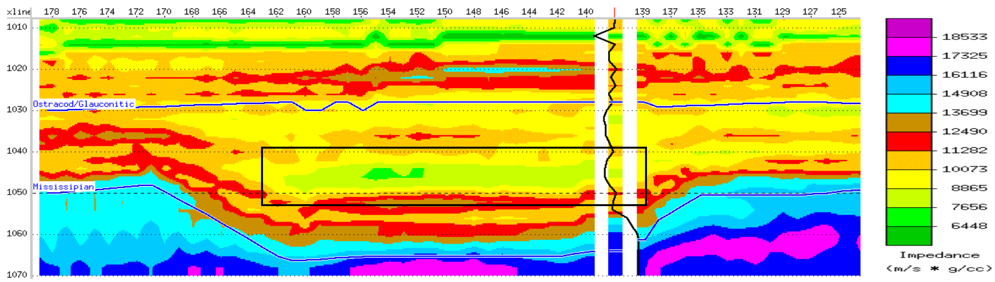
xline
Ostracod/Glauconitic
Mississipian
18533
17325
16116
14908
13699
12490
11282
10073
8865
7656
6448
Impedance
(m/s * g/cc)

(c)

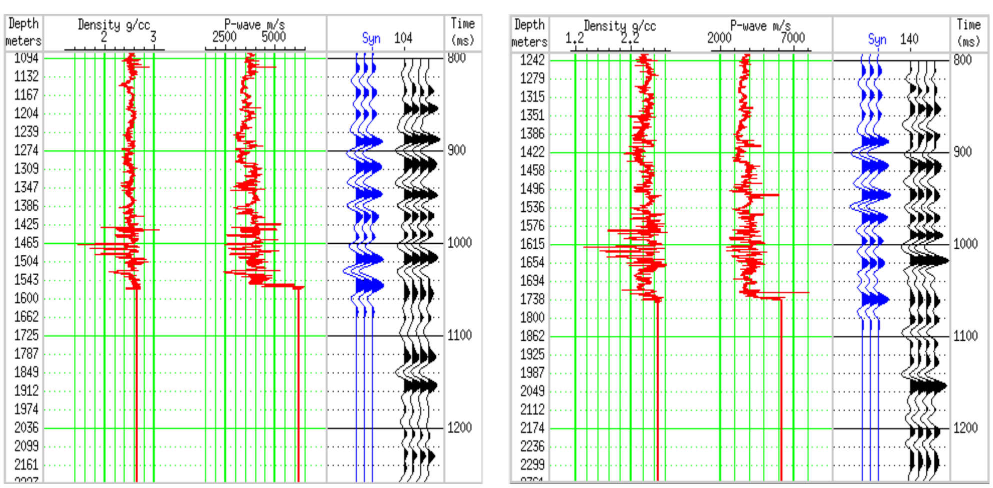
Depth meters
Density g/cc
P-wave m/s
Syn
104
Time (ms)
Depth meters
Density g/cc
P-wave m/s
Syn
140
Time (ms)

(d)

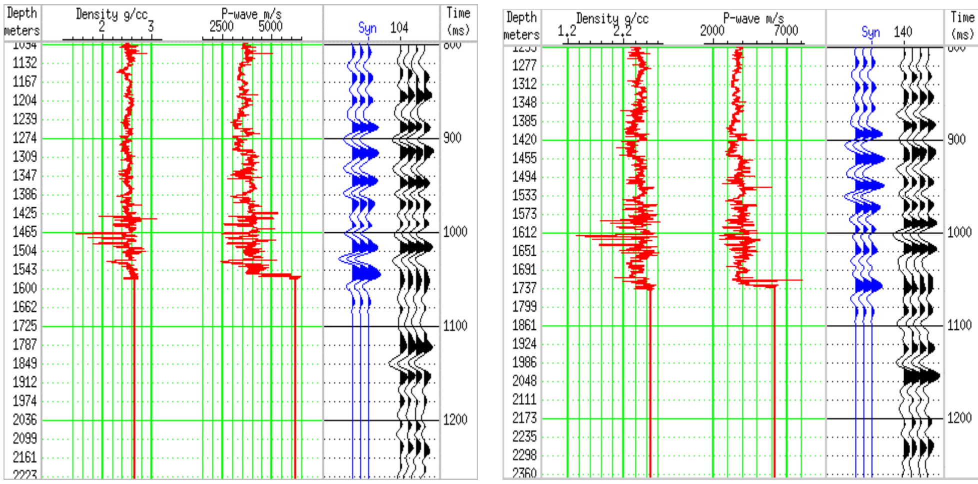

(e)

Figure 32. the inversion of zero offset stack section.

The inversion in Figure 32 is done by Hampson-Russell Strata. Although on panel (c) and panel (d) of Figure 32 the channel sand can be traced clearly, we must keep in mind the inversion results depend on wide band model building. However the correlation between seismic traces and synthetic traces on the zero offset stack are much superior to on the conversion stack.

CONCLUSIONS

Aki-Richards' approximation of P-S reflection coefficient has greater error than Aki-Richards' approximation of P-P reflection coefficient in the great property contrast cases, especially when S wave property changes a lot.

Aki-Richards' approximation of P-S coefficient is good for intermediate incident angle range and less changing S wave property.

The bulk modulus and shear modulus of dry rock are approximately equal and the gas bearing rock behaves as dry rock. The water saturation cause the bulk modulus increases rapidly. This determines the difference between the bulk modulus and shear modulus is very sensitive to the gas existing in the rocks.

P-S AVO extraction has more difficulties to be done than the P-P extraction because of the gather binning, statics, and noise levels.

Zero offset stack section has better resolution than conventional stack section. And the inversion of zero offset section shows good correlation between well logs and seismic traces in the Blackfoot.

P-P and P-S reflection coefficients can be expressed as the contrasts of elastic parameters and be applied in the linear regression analysis. The extraction of elastic parameter from Blackfoot 10 Hz vertical shows the reasonable results.

FUTURE WORK

Because of the relative lower S/N ratio of radial data, the analysis is tougher. The statics on the radial component are greater than on the vertical component. The careful processing is necessary. Now the authors are making efforts to process the Blackfoot data to obtain the high quality data to be used to AVO extraction.

In the meantime, the AVO inversion is considering to be employed as another approach. We would like the elastic earth model reconstruction by inversion. The converted wave information may help to constrain the inversion.

ACKNOWLEDGMENTS

We would like to thank sponsors of CREWES Project.

Thank Henry Bland and Darren Foltinek for their technical assistant in completing the project.

REFERENCES

Aki, K. I. and Richards, P. G., 1980, Quantitative seismology: W.H. Freeman and CO.

Behle, A. and Dohr, G. 1985, Converted waves in exploration seismic *in* Seismic Shear Waves, G. Dohr (ed.), 178-220. *Handbook of Geophysical Exploration*, Vol. 15b. Geophysical Press.

Bortfeld, R., 1961, Approximation to the reflection and transmission coefficients of plane longitudinal and transverse waves: Geophys. Prosp., 9, 485 - 502.

Castagna, J. P., Batzle, M. L. and Eastwood, R. L., 1985, Relationship between compressional wave and shear wave velocities in clastic silicate rocks: Geophysics, V. 50, 571 - 581.

Castagna, J. P., 1993, Petrophysical imaging using AVO: The Leading Edge, March, 1993, 172-178.

Castagna, J. P., Batzle, M. L. and Kan, T. K., 1993, Rock physics: the link between rock properties and AVO response *in* Castagna, J. P., and Backus, M. M., Eds., Offset-dependent reflectivity--Theory and practice of AVO analysis, Soc. Expl. Geophys., 135-171.

Chiburis, E., F., 1993, AVO applications in Saudi Arabia *in* Castagna, J. P., and Backus, M. M., Eds., Offset-dependent reflectivity--Theory and practice of AVO analysis, Soc. Expl. Geophys., 211-229.

Chung, W. Y., and Corrigan, D., 1985, Gathering mode-converted shear waves: a model study: 55th SEG meeting, Washington, Expanded Abstracts, 602-604.

Dahl, T., and Ursin, B., 1991, Parameter estimation in a one-dimensional anelastic medium, Journal of Geophysical Research, V 96, 20,217 - 20, 233.

Dey-Sarkar, S. K., and Svatek, S. V., Prestack analysis – An integrated approach for seismic interpretation in Clastic basins *in* Castagna, J. P., and Backus, M. M., Eds., Offset-dependent reflectivity--Theory and practice of AVO analysis, Soc. Expl. Geophys., 57-77.

Ferguson, R. J., P-P and P-S inversion of 3-C seismic data: Blackfoot, Alberta: CREWES Research Report 1995, Chapter 41.

Goodway, B., Chen, T., and Downton, J., 1997, Improved AVO fluid detection and lithology discrimination using Lame petrophysical parameters; “$\lambda\rho$”, “$\mu\rho$”, and “λ/μ fluid stack”, from P and S inversions: CSEG national convention, Expanded Abstracts, 148-151.

Goodway, B., Chen, T., and Downton, J., 1997, Improved AVO fluid detection and lithology discrimination using Lame petrophysical parameters; “$\lambda\rho$”, “$\mu\rho$”, and “λ/μ fluid stack”, from P and S inversions: 67th Ann. Internat. Mtg., Soc. Expl. Geophys., Expanded Abstracts.

Garotta, R., 1988, Amplitude-versus-offset measurements involving converted waves: 58th Ann. Internat. Mtg., Soc. Expl. Geophys., Expanded Abstracts, 1357.

Hampson, D., and Russell, B., 1990, AVO inversion: theory and practice: 60th Ann. Internat. Mtg., Soc. Expl. Geophys., Expanded Abstracts, 1456-1458.

Koefoed, O., 1955, On the effect of Poisson's ratio of rock strata on the reflection coefficients of plane waves: Geophs. Prosp., 3, 381-387.

Lindseth, R. O., 1979, Synthetic sonic logs -- a processing for stratigraphic interpretation: Geophysics, V. 44, No 1, 3 -26.

Margrave, G. F., Foltinek, D. S., 1995, P-P and P-SV cross sections: CREWES Research Report 1995, Chapter 5.

Miller, S. L. M., Aydemir, E. O., and Margrave, G. F., 1995, Preliminary interpretation of P-P and P-S seismic data from the Blackfoot broad-band survey: CREWES Research Report 1995, Chapter 42.

Parson, R., 1986, Estimating reservoir mechanical properties using constant offset images of reflection coefficients and incident angles: 56th Ann. Internat. Mtg., Expanded Abstracts, 617-620.

Pigott, J. D., Shrestha, R. K., and Warwick, R. A., 1990, Direct determination of Carbonate reservoir porosity and pressure from AVO inversion: 60^{th} Ann. Internat. Mtg., Soc. Expl. Geophys., Expanded Abstracts, 1533-1536.

Potter, C. C., Miller, S. L. M., and Margrave, G. F., 1995, Formation elastic parameters and synthetic P-P and P-S seismograms for the Blackfoot field: CREWES Research Report 1995, Chapter 37.

Rutherford, S. R. and Williams, R. H., 1989, Amplitude-versus-offset variation in gas sands: Geophysics, 54, 680-688.

Simin, V., Margrave, G. F., and Yang G. Y. C., AVO measurements for P-P and P-S data in Blackfoot 3C-3D dataset: CREWES Research Report 1995, Chapter 42.

Smith, G. C., and Gidlow, P. M., 1987, Weighted stacking from rock property estimation and detection of gas: Geophys. Prosp. 35, 993-1014.

Spratt, R. S., Goins, N. R., and Fitch, T. J., 1993, Pseudo-shear: The analysis of AVO *in* Castagna, J. P., and Backus, M. M., Eds., Offset-dependent reflectivity--Theory and practice of AVO analysis, Soc. Expl. Geophys., 37-56.

Shuey, R. T. 1985, A simplification of the Zoeppritz equations: Geophysics, V 50, 609 - 614.

Stewart, R. R., Zhang, Q., and Guthoff, F., 1995, Relationships among elastic-wave values (R^{pp}, R^{ps}, R^{ss}, V_p, V_s, ρ, σ, κ): CREWES Research Report 1995, Chapter 10.

Swan, H. W., 1991, Amplitude-versus-offset measurement errors in a finely layered medium: Geophysics, 56, 41-49.

Taylor, G., The point of P-S mode-converted reflection: An exact determination: Geophysics, 54, 1060-1063.

Tessmer, G., and Behle, A., 1988, Common reflection point data-stacking technique for converted waves: Geophys. Prosp., V 36, 671-688.

Verm, R. W., and Hilterman, F. J., 1994, Lithologic color-coded sections by AVO cross plots: The Leading Edge, August, 847 - 853.

Yu, G., 1985, Offset-amplitude variation and controlled-amplitude processing: Geophysics, 50, 2697-2708.

Zheng, X., 1992, United formulas for reflection and transmission in potential: Presented at the 62nd Annual International SEG Meeting, New Orleans, abstr. book, 1282-1284.

Zhong, B., Zhou, X., Liu, X., and Jiang, Y., A new strategy for CCP stacking: Geophysics, 60, 517-521.

APPENDIX

Zoeppritz equations of P-P and P-S reflection coefficients

Aki and Richards (1980) give the Knot-Zoeppritz equations in convenient forms. For completeness the reflection coefficients of the incident P wave and reflected P wave and S wave are shown as follows:

$$PP = [(b\frac{\cos i_1}{\alpha_1} - c\frac{\cos i_2}{\alpha_2})F - (a + d\frac{\cos i_1}{\alpha_1}\frac{\cos j_1}{\beta_1})Hp^2]/\mathrm{D}$$

$$PS = -2\frac{\cos i_1}{\alpha_1}(ab + cd\frac{\cos i_2}{\alpha_2}\frac{\cos j_2}{\beta_2})p\alpha_1/(\beta_1\mathrm{D})$$

where

$$\mathrm{M} = \begin{pmatrix} -\alpha_1 p & -\cos j_1 & \alpha_2 p & \cos j_2 \\ \cos i_1 & -\beta_1 p & \cos i_2 & -\beta_2 p \\ 2\rho_1\beta_1^2 p\cos i_1 & \rho_1\beta_1(1-2\beta_1^2 p^2) & 2\rho_2\beta_2^2 p\cos i_2 & \rho_2\beta_2(1-2\beta_2^2 p^2) \\ -\rho_1\alpha_1(1-2\beta_1^2 p^2) & 2\rho_1\beta_1^2 p\cos j_1 & \rho_2\alpha_2(1-2\beta_2^2 p^2) & -2\rho_2\beta_2^2 p\cos j_2 \end{pmatrix}$$

$$a = \rho_2(1-2\beta_2^2 p^2) - \rho_1(1-2\beta_1^2 p^2),\ b = \rho_2(1-2\beta_2^2 p^2) + 2\rho_1\beta_1^2 p^2,$$

$$c = \rho_1(1-2\beta_1^2 p^2) + 2\rho_2\beta_2^2 p^2,\ d = 2(\rho_2\beta_2^2 - \rho_1\beta_1^2),$$

$$E = b\frac{\cos i_1}{\alpha_1} + c\frac{\cos i_2}{\alpha_2},\ F = b\frac{\cos j_1}{\beta_1} + c\frac{\cos j_2}{\beta_2},$$

$$G = a - d\frac{\cos i_1}{\alpha_1}\frac{\cos j_2}{\beta_2},\ H = a - d\frac{\cos i_2}{\alpha_2}\frac{\cos j_1}{\beta_1},$$

and

$$\mathrm{D} = EF + GHp^2 = (\det\mathrm{M})/(\alpha_1\alpha_2\beta_1\beta_2).$$

The angles of i_1, i_2, j_1, and j_2 are shown on Figure A-1.

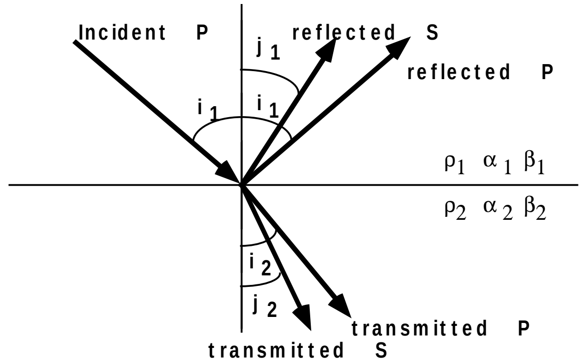

Figure A-1. Waves generated at an interface by an incident P-wave